Mon. Not. R. Astron. Soc. **373,** 45–64 (2006) doi:10.1111/j.1365-2966.2006.11049.x

Reconstructed density and velocity fields from the 2MASS Redshift Survey

Pirin Erdoğdu,[1,2,3⋆] Ofer Lahav,[3,4] John P. Huchra,[5]† Matthew Colless,[6] Roc M. Cutri,[7] Emilio Falco,[5]† Teddy George,[6] Thomas Jarrett,[8] D. Heath Jones,[7] Lucas M. Macri,[9] Jeff Mader,[10] Nathalie Martimbeau,[5] Michael A. Pahre,[5] Quentin A. Parker,[7,11] Anaïs Rassat[4] and Will Saunders[7]

[1]*Department of Physics, Middle East Technical University, 06531 Ankara, Turkey*
[2]*School of Physics & Astronomy, University of Nottingham, University Park, Nottingham NG7 2RD*
[3]*Institute of Astronomy, Madingley Road, Cambridge CB3 0HA*
[4]*Department of Physics and Astronomy, University College London, Gower Street, London WC1E 6BT*
[5]*Harvard–Smithsonian Center for Astrophysics, 60 Garden Street, MS-20, Cambridge, MA 02138, USA*
[6]*Canada–France–Hawaii Telescope Corporation, 65-1238 Mamalahoa Hwy Kamuela, HI 96743, USA*
[7]*Anglo-Australian Observatory, PO Box 296, Epping, NSW 2052, Australia*
[8]*Infrared Processing and Analysis Center, California Institute of Technology, Pasadena, CA 91125, USA*
[9]*National Optical Astronomy Observatory, 950 North Chrry Avenue, Tucson, AZ 85726, USA*
[10]*W. M. Keck Observatory, Kamuela, HI 96743, USA*
[11]*Department of Physics, Macquarie University, Sydney, NWS 2109, Australia*

Accepted 2006 September 4. Received 2006 August 30; in original form 2006 May 9

ABSTRACT

We present the reconstructed real-space density and the predicted velocity fields from the Two-Micron All-Sky Redshift Survey (2MRS). The 2MRS is the densest all-sky redshift survey to date and includes about 23 200 galaxies with extinction-corrected magnitudes brighter than $K_s = 11.25$. Our method is based on the expansion of these fields in Fourier–Bessel functions. Within this framework, the linear redshift distortions only affect the density field in the radial direction and can easily be deconvolved using a distortion matrix. Moreover, in this coordinate system, the velocity field is related to the density field by a simple linear transformation. The shot noise errors in the reconstructions are suppressed by means of a Wiener filter which yields a minimum variance estimate of the density and velocity fields. Using the reconstructed real-space density fields, we identify all major superclusters and voids. At 50 h^{-1} Mpc, our reconstructed velocity field indicates a backside infall to the Great Attractor region of $v_{\rm infall} = (491 \pm 200)\,(\beta/0.5)\,{\rm km\,s^{-1}}$ in the Local Group frame and $v_{\rm infall} = (64 \pm 205)\,(\beta/0.5)\,{\rm km\,s^{-1}}$ in the cosmic microwave background (CMB) frame and β is the redshift distortion parameter. The direction of the reconstructed dipole agrees well with the dipole derived by Erdoğdu et al. The misalignment between the reconstructed 2MRS and the CMB dipoles drops to 13° at around 5000 km s^{-1} but then increases at larger distances.

Key words: surveys – galaxies: distances and redshifts – cosmology: observations – large-scale structure of Universe.

1 INTRODUCTION

A cosmographical description of the galaxy distribution is crucial to our understanding of the mechanisms of structure formation that generate the complex pattern of sheets and filaments comprising the 'cosmic web'. Today, there are many more redshifts available for galaxies than velocity measurements. This discrepancy has inspired a great deal of work on methods for the reconstruction of the mass and velocity fields from redshifts alone. These methods use a variety of functional representations (e.g. Cartesian, Fourier, spherical harmonics or wavelets) and smoothing techniques (e.g. a Gaussian or a top-hat sphere). However, several complications arise when one tries to reconstruct peculiar velocity and real-space mass density fields directly from redshift surveys. First, one must relate the light distribution to the mass field. On large scales, this

⋆E-mail: pirin.erdogdu@nottingham.ac.uk
†Guest Observer, Cerro Tololo Interamerican Observatory, operated by AURA for the National Science Foundation.

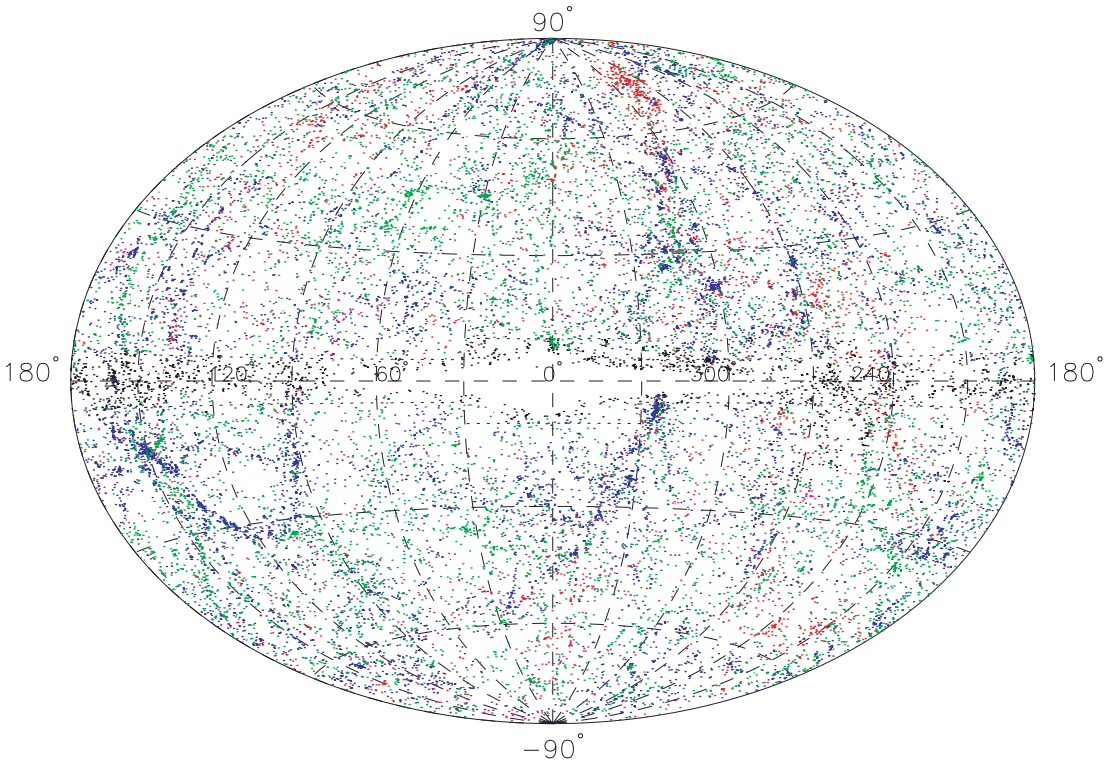

Figure 1. All Objects (24 788 galaxies) in the 2MASS Redshift Catalogue in Galactic Aitoff projection. The plot contains galaxies with $z \leqslant 0.01$ plotted in red, $0.01 < z \leqslant 0.025$ are plotted in blue, $0.025 < z < 0.05$ are plotted in green and $z \geqslant 0.05$ are plotted in magenta. Galaxies without measured redshifts are plotted in black. The zone of avoidance is outlined by dashed lines.

relationship is generally assumed to be linear with a proportionality constant (but see e.g. Conway et al. 2005; Marinoni et al. 2005; Wild et al. 2005, who argue that biasing is non-linear and redshift dependent even on large scales). Another common assumption is that the galaxy distribution samples the underlying smooth mass field and the finite sampling of the smooth field introduces Poisson 'shot noise' errors.[1] Yet another important physical problem associated with the recovery of the real-space mass density field from the galaxy density field is the correction of the distortions in the redshift-space clustering pattern. Furthermore, in redshift surveys the actual number of galaxies in a given volume is larger than the number observed, particularly in flux-limited samples where at large distances only the very luminous galaxies can be seen.

In this paper, we recover the real-space density and predicted velocity fields of the Two-Micron All-Sky Redshift Survey (2MRS) (Huchra et al. 2005). The reconstruction procedure used is based on linear theory and closely follows Fisher et al. (1995; hereafter FLHLZ). The density field in redshift space is decomposed into spherical harmonics and Bessel functions (Fourier–Bessel functions). Then the real-space density and velocity fields are reconstructed from those in the redshift space using a Wiener filter.

The idea of cosmography using spherical harmonics goes back to Peebles (1973), but the method only gained popularity with the advent of all-sky surveys. Since then, it has been applied to the *Infrared Astronomical Satellite* (*IRAS*) selected galaxy surveys [e.g. to the *IRAS* 1.2-Jy survey by Fabbri & Natale 1990; Scharf et al. 1992; Scharf & Lahav 1993; Fisher, Scharf & Lahav 1994; Lahav et al. 1994; Nusser & Davis 1994; Heavens & Taylor 1995 and to *IRAS* Point Source Catalogue Redshift Survey (PSCz) by Tadros et al. 1999; Hamilton, Tegmark & Padmanabhan 2000; Taylor et al. 2001] and the peculiar velocity catalogues (e.g. to elliptical galaxy sample by Regs & Szalay 1989; to Mark III galaxy sample by Davis, Nusser & Willick 1996 and Hoffman, Eldar & Zaroubi 2001). The spherical harmonics technique has proven to be very convenient for addressing many of the problems inherent to the analyses of redshift surveys.

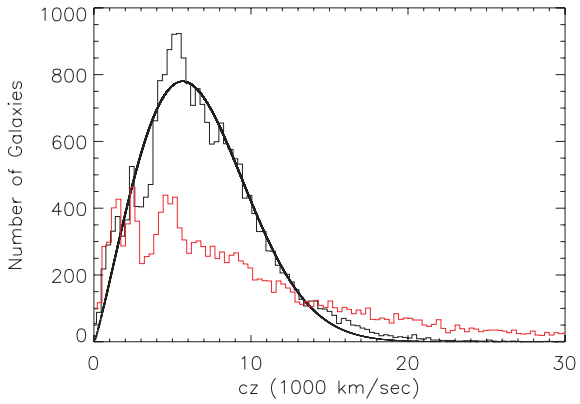

Figure 2. Redshift histogram for 2MRS galaxies and a least-squares fit (equation 2) to the data (black). For comparison, also plotted is a redshift histogram for PSCz galaxies (Saunders et al. 2000) (red).

[1] This is only an approximation. A more realistic model for galaxy clustering is the halo model (e.g. Cooray & Sheth 2002) where the linear bias parameter depends on the mass of the dark matter haloes where the galaxies reside. For this model, the mean number of galaxy pairs in a given halo is usually lower than the Poisson expectation.

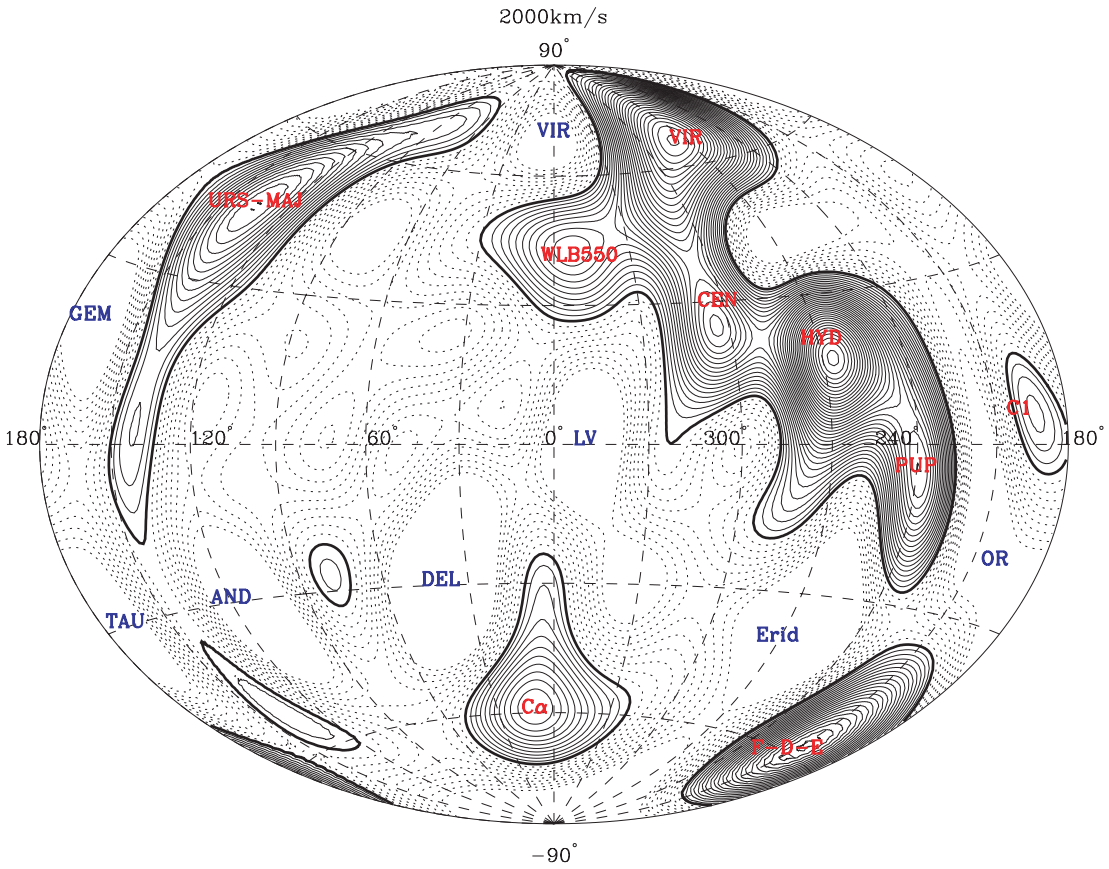

Figure 3. The reconstructed density field, evaluated on a thin shell at 2000 km s^{-1}, shown in Galactic Aitoff projection. Dashed lines show $\delta < 0$, and solid lines show $\delta \geqslant 0$, with contour spacing $\}\Delta\,\delta\} = 0.1$. The overdense regions are (from left to right) Ursa Major (Urs Maj), WLB 550, C α, Virgo (Vir), Centaurus (Cen), Hydra (Hyd), Puppis (Pup), Fornax–Doradus–Eridanus (F–D–E) and C1. The voids are Gemini (Gem), Taurus (Tau), Andromeda (And), Delphinus (Del), Virgo (Vir), Local Void (LV), Eridanus (Erid) and Orion (Or).

The spherical harmonics are one of the most convenient ways of smoothing the noisy data. A careful choice of spherical coefficients greatly reduces the statistical uncertainties and errors introduced by the non-linear effects. Furthermore, the treatment of linear redshift distortions is particularly straightforward in Fourier–Bessel space, especially for surveys which have almost all-sky coverage and dense sampling such as 2MRS.

The Wiener-filtered fields are optimal reconstructions in the sense that the variance between the derived reconstruction and the underlying true field is minimized. As opposed to ad hoc smoothing schemes, the smoothing due to the Wiener filter is determined by the data. In the limit of high signal-to-noise ratio, the Wiener filter modifies the observed data only weakly, whereas it strongly suppresses the contribution of the data contaminated by shot noise. The three-dimensional Wiener reconstruction of cosmological fields in Fourier–Bessel space was first developed by FLHLZ and applied to the *IRAS* 1.2-Jy survey. Webster, Lahav & Fisher (1997, hereafter WLF) expanded on the initial results of FLHLZ. Later, Schmoldt et al. (1999) applied the same method to the *IRAS* PSCz survey to recover density and velocity fields.

This paper is structured as follows. In the next section, we describe the 2MRS. In Section 3, we give a brief summary of the decomposition of the density field in redshift space into a set of orthogonal spherical harmonics and Bessel functions. In Section 4, we discuss how these redshift-space harmonics are related to those in real space. In Section 5, we give expressions for the Wiener filter in Fourier–Bessel space. The implementation of the method to 2MRS is given in Section 6, along with the maps of the density and velocity fields. In the same section, we also show reconstruction of the Local Group (LG) acceleration determined directly from harmonic coefficients. The last section contains a discussion and summary of the work. Throughout this paper, we assume that the galaxy distribution is related to the underlying smooth mass density field by the linear bias parameter, b, so that $\delta_{\rm g}(\boldsymbol{x}) = b\delta_{\rm m}(\boldsymbol{x})$. With this notation, the constant of proportionality between velocity and the density field is β, where $\beta = {\Omega_{\rm m}}^{0.6}/b$. It is worth emphasizing that one of the ultimate goals of this work is to test linear biasing by comparing the reconstructed velocity fields with the observed peculiar velocity field. The distances are given in units of velocity and the Hubble constant is $H_0 = 100\,h\,{\rm km\,s^{-1}\,Mpc^{-1}}$.

2 THE 2MRS

The 2MRS is the densest all-sky redshift survey to date. The galaxies in the northern celestial hemisphere are being observed by the Fred Lawrence Whipple Observatory (FLWO) 1.5-m telescope, the Arecibo 305-m telescope and the Green Bank 100-m telescope. In the Southern hemisphere, most galaxies at high galactic latitude (about 6000 galaxies) were observed as a part of the

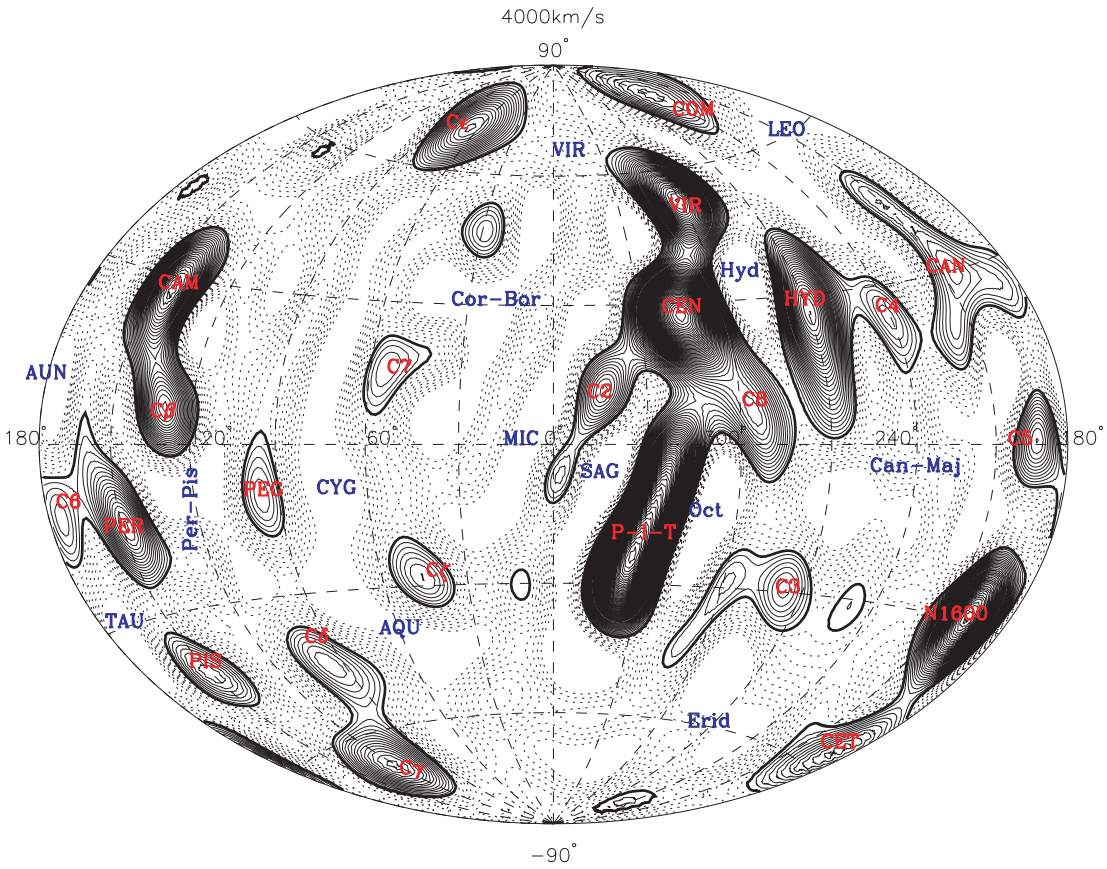

Figure 4. Same as Fig. 3 but evaluated at 4000 km s^{-1}. The overdense regions are C6, Perseus (Per), Pisces (Pis), Camelopardalis (Cam), Cβ, Pegasus (Peg), Cδ, Cγ, Cϵ, C7, Cζ, C2, Coma (Com), Virgo (Vir), Centaurus (Cen), Pavo–Indus–Telescopium (P–I–T), C8, Hydra (Hyd), C3, C4, Cancer (Can), NGC 1600 (N1600), Cetus (Cet) and C5. The voids are Aunga (Aun), Taurus (Tau), Perseus–Pisces (Per–Pis), Cygnus (Cyg), Aquarius (Aqu), Corona Borealis (Cor Bor), Microscopium (Mic), Virgo (Vir), Sagittarius (Sag), Hydra (Hyd), Octans (Oct), Leo, Eridanus (Erid) and Canis Major (Can Maj).

6-degree Field Galaxy Survey[2] (6dFGS; Jones et al. 2004, 2005) and the low galactic latitude galaxies are being observed at CTIO (by L. Macri and J. P. Huchra). The first phase of 2MRS is now complete. In this phase, we obtained redshifts for approximately 23 150 Two-Micron All-Sky Survey (2MASS) galaxies from a total sample of 24 773 galaxies with extinction-corrected magnitudes (Schlegel, Finkbeiner & Davis 1998) brighter than $K_s = 11.25$. This magnitude limit corresponds to a median redshift of $z \approx 0.02$ (≈ 6000 km s^{-1}). Almost all of the 1600 galaxies that remain without redshifts are at very low galactic latitudes ($|b| \lesssim 5^\circ$) or obscured/confused by the dust and the high stellar density towards the Galactic Centre. Fig. 1 shows all the objects in 2MRS in Galactic Aitoff projection. Galaxies with $z \leqslant 0.01$ are plotted in red, $0.01 < z \leqslant 0.025$ are plotted in blue, $0.025 < z < 0.05$ are plotted in green and $z \geqslant 0.05$ are plotted in magenta. Galaxies without measured redshifts are plotted in black. 2MRS can be compared with the deeper 2MASS galaxy catalogue (K < 14th mag) shown in Jarrett (2004, fig. 1).

[2] 6dFGS has a much fainter magnitude limit ($K_s = 12.75$) than 2MRS and contains around 150 000 galaxy redshifts. The 6dFGS documentation and the data base can be found on the WWW at http://www.aao.gov.au/local/www/6df/

2.1 Survey completeness

2MASS[3] has good photometric uniformity and an unprecedented integral sky coverage. The photometric uniformity is better than 4 per cent over the sky including the celestial poles (e.g. Jarrett et al. 2000a; Jarrett et al. 2003) and at magnitudes brighter than $K_s = 12$, 2MASS is essentially complete down to very low galactic latitudes (to $b^2\circ$; e.g. Huchra et al. 2005). The uniform completeness of the galaxy sample is slightly limited by the presence of foreground stars, for a typical high-latitude sky less than 2 per cent of the area is masked. These missing regions are accounted for using a coverage map, defined as the fraction of the area of an 8×8 arcmin^2 pixel that is not obscured by stars brighter than 10th mag. Galaxies are then weighted by the inverse of the completeness, although the analysis is almost unaffected by this process as the completeness ratio is very close to one for most parts of the sky.

The stellar contamination of the catalogue is low and is reduced further by manually inspecting the objects below a heliocentric redshift of $cz = 200$ km s^{-1}. The foreground stellar confusion is highest at low Galactic latitudes, resulting in decreasing overall completeness of the 2MASS catalogue (e.g. Jarrett et al. 2000b) and

[3] 2MASS data base and the full documentation are available on the WWW at http://www.ipac.caltech.edu/2mass.

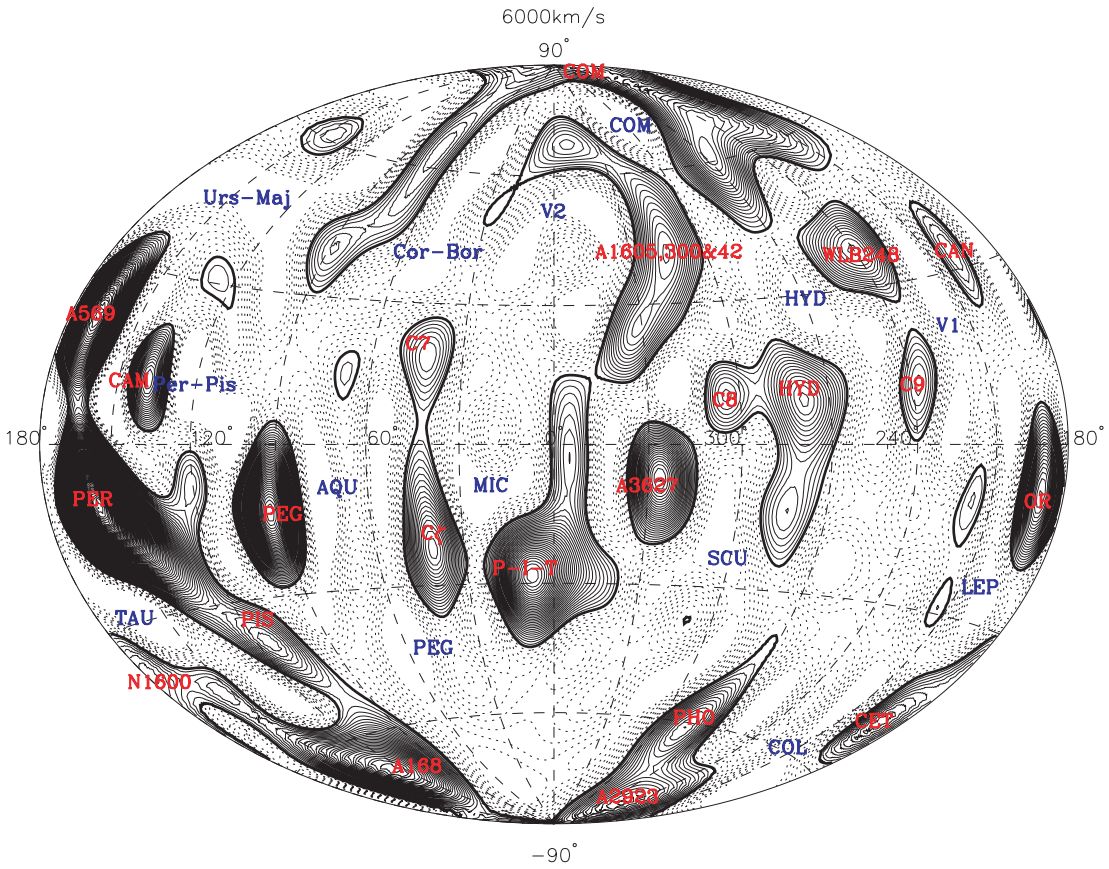

Figure 5. Same as in Fig. 3 but evaluated at 6000 km s^{-1}. The overdensities are Abell 569 (A569), Perseus (Per), Pisces (Pis), NGC 1600 (N1600), Abell 168, Camelopardalis (Cam), Pegasus (Peg), C7, Cζ, Pavo–Indus–Telescopium (P–I–T), Abell Clusters 1605, 300 & 42, Abell 3627, C8, Phoenix (Pho), Abell 2923, Coma (Com), Hydra (Hyd), WLB 248, C9, Cancer (Can), Orion (Or) and Cetus (Cet). The voids are Taurus (Tau), Ursa Major (Urs Maj), Perseus–Pisces (Per–Pis), Aquarius (Aqu), Corona–Borealis (Cor–Bor), Pegasus (Peg), V2, Microscopium (Mic), Coma (Com), Sculptor (Scu), Columba (Col), V1 and Lepus (Lep).

consequently the 2MRS sample. Stellar confusion also produces colour bias in the 2MASS galaxy photometry (Cambrésy, Jarrett & Beichman 2005), but this bias should not be significant for 2MRS due to its relatively bright magnitude limit.

2.2 Magnitude and flux conversions

2MRS uses the 2MASS magnitude K_{20}, which is defined[4] as the magnitude inside the circular isophote corresponding to a surface brightness of $\mu_{K_s} = 20$ mag arcsec^{-2} (e.g. Jarrett et al. 2000a). The isophotal magnitudes underestimate the total luminosity by 10 per cent for the early-type and 20 per cent for the late-type galaxies (Jarrett et al. 2003). Following Kochanek et al. (2001, appendix), an offset of $\Delta = -0.20 \pm 0.04$ is added to the K_{20} magnitudes. The galaxy magnitudes are corrected for Galactic extinction using the dust maps of Schlegel et al. (1998) and an extinction correction coefficient of $R_K = 0.35$ (Cardelli, Clayton & Mathis 1989). As expected, the extinction corrections are small for the 2MRS sample. The K_s-band k-correction is derived by Kochanek et al. (2001) based on the stellar population models of Worthey (1994). The k-correction of $k(z) = -6.0 \log(1 + z)$, is independent of galaxy type and valid for $z \lesssim 0.25$.

[4] Column 17 (k_m_k20fc) in the 2MASS in the Extended Source Catalogue (XSC).

The flux, S, for each galaxy is computed from the apparent magnitudes using

$$S = S(0\,\mathrm{mag})10^{-0.4(K_{20}+\mathrm{ZPO})}, \quad (1)$$

where the zero-point offset is ZPO $= 0.017 \pm 0.005$ and $S(0\,\mathrm{mag}) = 1.122 \times 10^{-14} \pm 1.891 \times 10^{-16}$ W cm^{-2} for the K_s band (Cohen, Wheaton & Megeath 2003).

2.3 The redshift distribution and the selection function

The redshift distribution of 2MRS is shown in Fig. 2. The *IRAS* PSCz survey redshift distribution (Saunders et al. 2000) is also plotted for comparison. 2MRS samples the galaxy distribution better than the PSCz survey out to $cz = 15\,000$ km s^{-1}. The selection function of the survey (i.e. the probability of detecting a galaxy as a function of distance) is modelled using a parametrized fit to the redshift distribution:

$$\mathrm{d}N(z) = Az^{\gamma} \exp\left[-\left(\frac{z}{z_c}\right)^{\alpha} \right] \mathrm{d}z, \quad (2)$$

with best-fitting parameters of $A = 116\,000 \pm 4000, \alpha = 2.108 \pm 0.003, \gamma = 1.125 \pm 0.025$ and $z_c = 0.025 \pm 0.001$. This best fit is also shown in Fig. 2 (solid line). The overall selection function $\phi_s(r)$

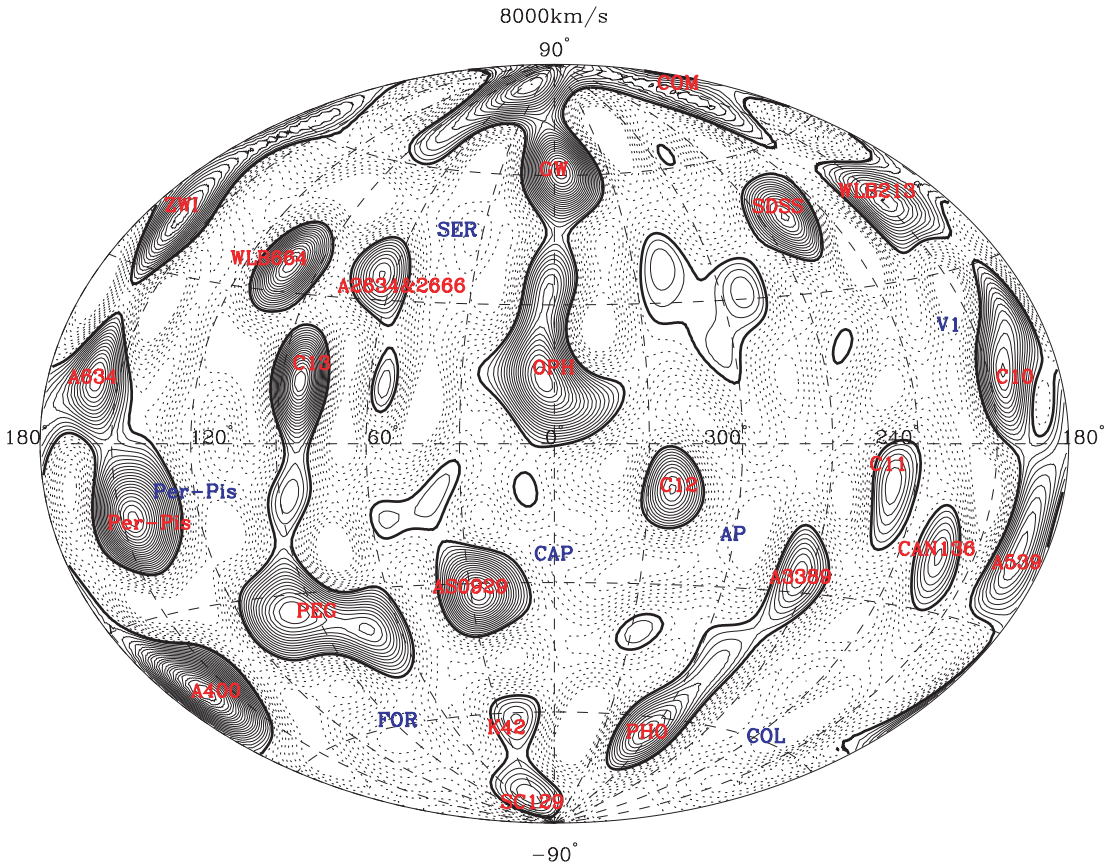

Figure 6. Same as in Fig. 3 but evaluated at 8000 km s^{-1}. The overdensities are ZwCl 0943.7+5454 (ZWI), Abell 634, Perseus–Pisces (Per–Pis), Abell 400, WLB 664, C13, Pegasus (Peg), Abell Clusters 2634 & 2666, Abell S0929, Klemola 42 (K42), Great Wall (GW), Ophiuchus (Oph), SC 129, C12, Phoenix (Pho), Coma (Com), SDSS CE J159.778641−00.784376 (SDSS), Abell 3389, WLB 213, C11, CAN 136, C10 and Abell 539. The voids are Perseus–Pisces (Per–Pis), Fornax (For), Serpens (Ser), Capricornus (Cap), Apus (Ap), Columba (Col) and V1.

is the redshift distribution divided by the volume element

$$\phi_{\rm s}(r) = \frac{1}{\Omega_{\rm s} r^2} \left(\frac{{\rm d}N}{{\rm d}z}\right)_r \left(\frac{{\rm d}z}{{\rm d}r}\right)_r , \qquad (3)$$

where $\Omega_{\rm s} (\approx 4\pi$ sr) is the solid angle of the survey and r is the comoving distance.

3 EXPANSION OF THE DENSITY, VELOCITY AND GRAVITATIONAL POTENTIAL FIELDS IN SPHERICAL HARMONICS

This section describes the spherical harmonic expansion of the density and velocity fields. Spherical harmonics are commonly employed in cosmography of whole-sky surveys for two main reasons. First, separating the observed density field into angular and radial modes concentrates the linear scale redshift distortions into one dimension, making distortions easier to deconvolve. Secondly, both spherical harmonic and Bessel functions are orthogonal and together they form eigenfunctions of the Laplacian operator. These properties lead to very simple relationships between the density, the velocity and the potential fields in harmonic space, allowing the straightforward reconstruction of one field from another observed field. The method used in this paper is based on that developed by FLHLZ. Therefore, we do not give a full description of our method; we only outline the formalism.

3.1 Expansion of the density field

The density field, $\rho(\boldsymbol{r})$, can be expanded as a Fourier–Bessel series in the following way:

$$\rho(\boldsymbol{r}) = \sum_{l=0}^{l_{\rm max}} \sum_{m=-l}^{+l} \sum_{n=1}^{n_{\rm max}(l)} C_{ln}\, \rho_{lmn}\, j_l(k_n r)\, Y_{lm}(\theta, \phi)$$
$$= \sum_{lmn} C_{ln}\, \rho_{lmn}\, j_l(k_n r)\, Y_{lm}(\theta, \phi). \qquad (4)$$

Here, ρ_{lmn} is the density coefficient, $Y_{lm}(\theta, \phi)$ is the spherical harmonic corresponding to the spherical angular coordinates, $j_l(x)$ is the spherical Bessel function and C_{ln} is the normalization constant of the spherical Bessel function. The resolution of the angular modes is determined by the value of $l_{\rm max}$ and that of the radial modes by the value of $n_{\rm max}(l)$. In theory, $l_{\rm max}$ and $n_{\rm max}(l)$ tend to infinity. In practice, since the distances which galaxy surveys probe are finite, $l_{\rm max}$ and $n_{\rm max}(l)$ need to be truncated at finite numbers. This truncation is an effective smoothing of the density field and limits the resolution of the structure in the reconstruction such that the structures smaller than the effective resolution of the highest harmonic, $\Delta\theta \sim \pi/l_{\rm max}$ (cf. Peebles 1980, section 46) and the highest radial mode, $\Delta r \sim \pi/k_{n_{\rm max}}$, will be lost. On the other hand, if the expansion is continued to a very high order the resolution of expansion will be higher than the size of the real structure, introducing artefacts into the reconstruction of density field. The choice of $l_{\rm max}$ and $n_{\rm max}(l)$ is discussed in Section 6.

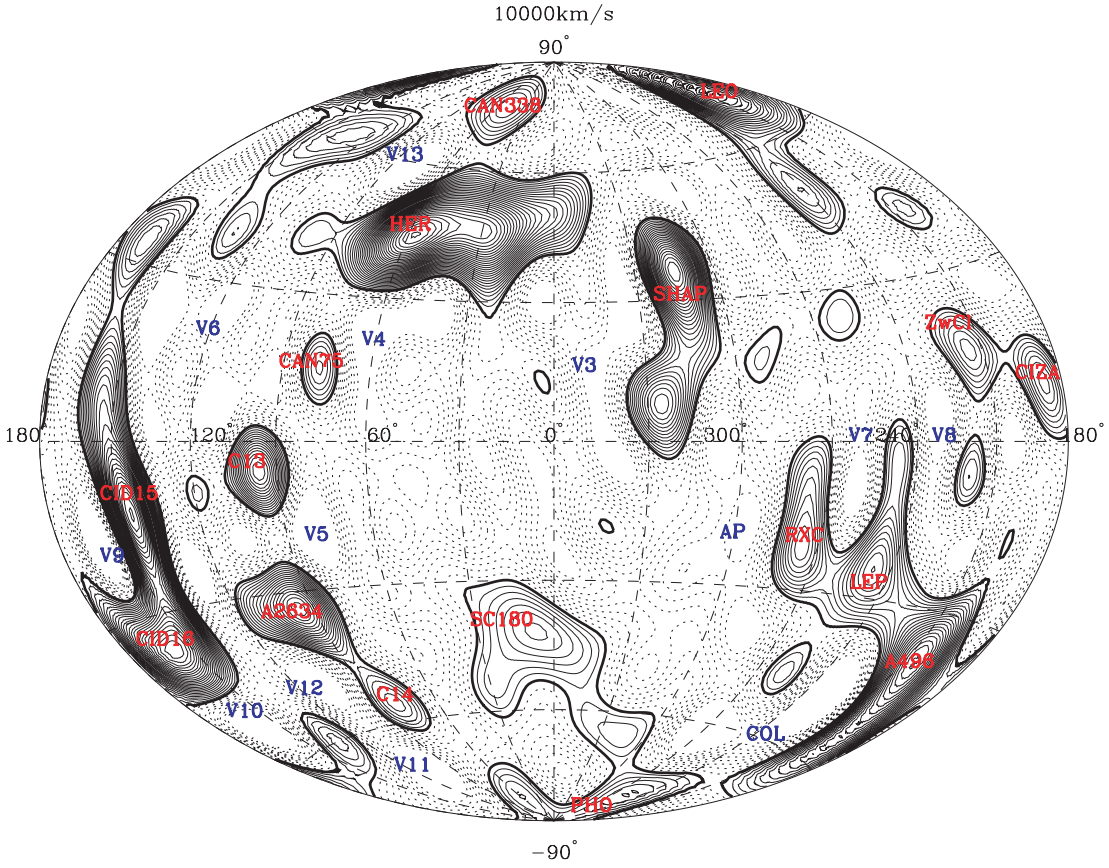

Figure 7. Same as in Fig. 3 but evaluated at 10 000 km s^{-1}. The overdensities are CID 15, CID16, C13, Abell 2634, C14, CAN 75, CAN 338, Hercules (Her), SC180, Shapley (Shap), Phoenix (Pho), Leo, RXC J0712.0−6030, Lepus (Lep), ZwCl 0820.6+0436, Abell 496 and CIZA J0603.8+2939. The voids are V9, V6, V10, V12, V11, V13, V5, V4, V3, Apus (Ap), V7, Columba (Col) and V8.

The radial modes, k_n, correspond to a given angular mode l and the C_{ln}s are chosen according to the boundary conditions and to ensure the orthogonality of the spherical Bessel functions. It is assumed that the data are only given within a sphere of radius R and that the logarithmic derivative of the gravitational potential is continuous at $r = R$. The corresponding value of C_{ln} is $1/(\frac{R^3}{2}[j_l(k_n R)]^2)$. The derivation of this result is given in FLHLZ, appendix A.

Given that the data from a flux-limited redshift catalogue are a set of N discrete points with a redshift-space position vector $\boldsymbol{s}$ and a weighting function $w(s_i)$, the harmonic density coefficients in redshift space can be derived using the inversion formula

$$\rho^S_{lmn} = \sum_{i=1}^{N} w(s_i) j_l(k_n s_i) Y^*_{lm}(\theta_i, \phi_i), \tag{5}$$

where the superscripts S and R hereafter denote redshift and real space, respectively. We give each galaxy the weight $w(s_i) = 1/\phi_s(s_i)$ and $\phi_s(s_i)$ [$\approx \phi_s(r_i)$] is the selection function of galaxy i.

The density fluctuations, $\delta(\boldsymbol{s}) = [\rho(\boldsymbol{s})/\bar{\rho}] - 1$, can be estimated in terms of the Fourier–Bessel function

$$\delta^S_{lmn} = \frac{\rho^S_{lmn}}{\bar{\rho}} - \mathbf{M}_{lmn}, \tag{6}$$

where $\bar{\rho}$ is the mean density of the survey and the second term $\mathbf{M}_{lmn}$ represents a monopole correction (cf. FLHLZ, equation D14).

3.2 Expansion of the velocity field

The linear theory velocity field in spherical harmonics is given by Regs & Szalay (1989). It is derived by expanding the gravitational potential $\phi(\boldsymbol{r})$ and the density fluctuations $\delta(\boldsymbol{r})$ in Fourier–Bessel series, and substituting these into Poisson's equation. Since $j_l(k_n r)Y_{lm}(\theta, \phi)$ is an eigenfunction of the Laplacian operator,

$$\nabla^2[j_l(k_n r)Y_{lm}(\theta, \phi)] = -k_n^2 j_l(k_n r)Y_{lm}(\theta, \phi), \tag{7}$$

the harmonics of the gravity field can be related to those of the galaxy density field as

$$\phi_{lmn} = -\frac{3}{2}\Omega_{\rm m}^{0.6} H_0^2 \frac{\delta_{lmn}}{k_n^2}. \tag{8}$$

The radial component of the velocity field, $\boldsymbol{v}_\parallel(\boldsymbol{r}) = \hat{\boldsymbol{r}} \cdot \boldsymbol{v}(\boldsymbol{r})$, can be decomposed into harmonics as in equation (4). The harmonic coefficients v_{lmn} for the predicted radial velocity field within $r < R$ are derived by comparing the harmonic expansions of the velocity field and the gravitational potential field

$$v_{lmn} = \beta H_0 \sum_{n'} (\Xi_l)_{nn'} \left(\delta^R_{lmn'}\right), \tag{9}$$

with Ξ as the velocity matrix (cf. FLHLZ, equation 22).

In spherical harmonics, the LG velocity, $\boldsymbol{v}(\boldsymbol{0})$, is written as (see FLHLZ, appendix C1)

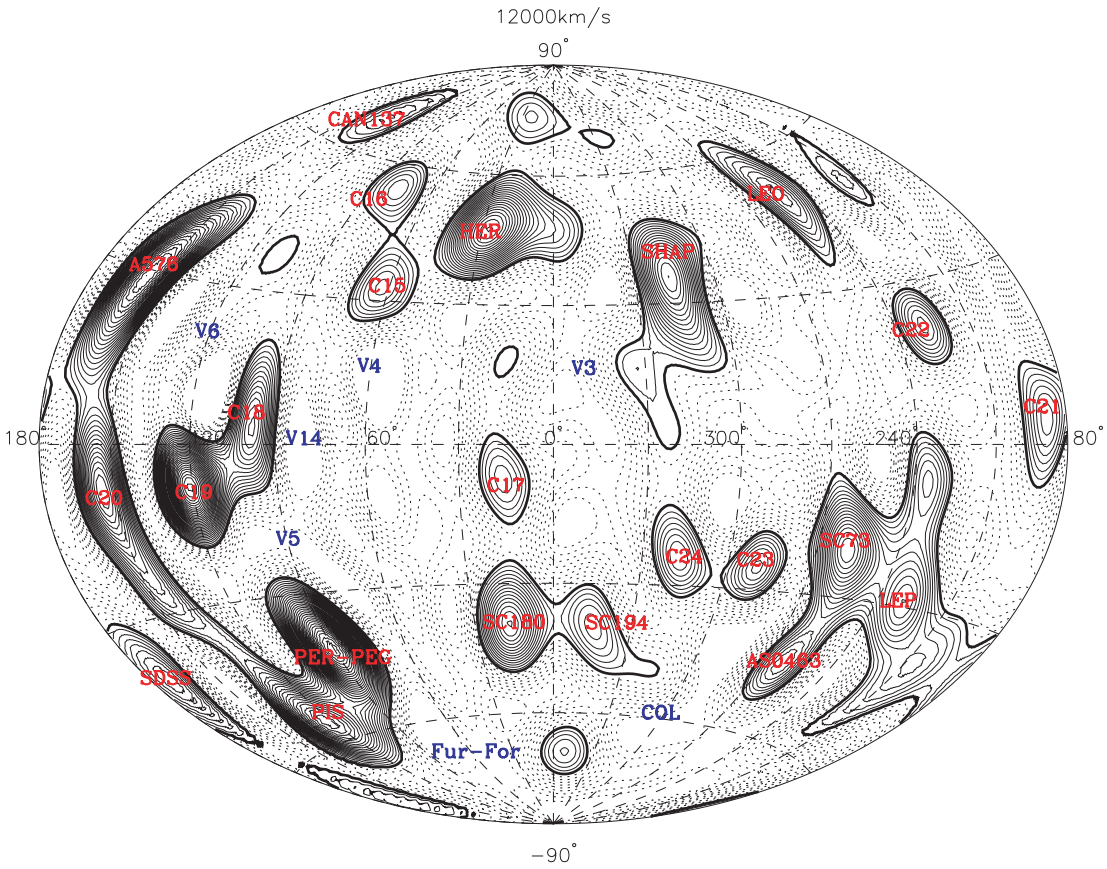

Figure 8. Same as in Fig. 3 but evaluated at 12 000 km s^{-1}. The overdensities are SDSS clusters SDSS CE J048.551922−00.613762 and SDSS CE J050.935932−00.117944 (SDSS), Abell 576, C20, Pisces (Pis), CAN 137, C19, C18, Perseus–Pegasus (Per–Peg), C16, C15, Hercules (Her), C17, SC180, SC194, Shapley (Shap), C24, C23, Leo, SC73, Abell S0463, C22, Lepus (Lep) and C21. The voids are V6, V14, V5, V4, Further–Fornax (Fur–For), V3 and Columba (Col).

$$\boldsymbol{v}(\mathbf{0}) = \frac{\beta H_0}{3\sqrt{4\pi}} \sum_{n=1}^{n_{\max}(l)} C_{1n} \int_0^R \mathrm{d}r'\, j_l(k_n r') \times \left(-\sqrt{2}\mathrm{Re}\left[\delta^R_{11n}\right] \boldsymbol{i} + \sqrt{2}\mathrm{Im}\left[\delta^R_{11n}\right] \boldsymbol{j} + \mathrm{Re}\left[\delta^R_{10n}\right] \boldsymbol{k}\right), \quad (10)$$

where Re[a] and Im[a] refer to the real and imaginary parts of a complex number, a, and R is the radius out to which the density field is measured for the calculation of the velocity.

The harmonics of the transverse velocity field ($\boldsymbol{v}_\perp = -\boldsymbol{r} \times [\boldsymbol{r} \times \boldsymbol{v}\,(\boldsymbol{r})]$) are also related to those of the density field. They can be derived using quantum mechanical methods (see FLHLZ, appendix C2).

4 DECONVOLVING REDSHIFT-SPACE DISTORTIONS IN SPHERICAL HARMONICS

The galaxy peculiar velocities will only introduce distortions in the radial direction, leaving the angular parts intact. Thus, if the density field in redshift space is expressed in terms of the orthogonal radial and the angular components, as it is the case in the Fourier–Bessel space, the redshift distortions will only couple the radial modes of the real-space density field. This coupling is described by a coupling matrix, $(\mathbf{Z}_l)_{nn'}$ (Fisher et al. 1994, and FLHLZ),

$$\delta^S_{lmn} = \sum_{n'=1}^{n_{\max}(l)} (\mathbf{Z}_l)_{nn'}\, \delta^R_{lmn'}, \quad (11)$$

where $(\mathbf{Z}_l)_{nn'}$ depends only on H_0, β, $w(r)$ and $\phi_s(r)$ and is independent of the power spectrum.[5] The full derivation of the coupling matrix is given in FLHLZ, appendix D. We note that equation (11) is calculated for linear scales only. On small scales, the peculiar velocities introduce radially extended distortions called *Fingers of God*. These distortions can be corrected for either by collapsing the fingers to a point at high-density regions or by assuming a Maxwellian distribution for the peculiar velocities (Peacock & Dodds 1994) and deconvolving this distribution from the reconstructed fields (Heavens & Taylor 1995; Erdoğdu et al. 2004). In any case, they will not change the constructed fields substantially as they are smoothed out due to the resolution of the spherical harmonics (see Erdoğdu et al. 2004, who use who a similar resolution).

In the absence of shot noise, the real-space density harmonics can simply be obtained by inverting the coupling matrix in equation (11). However, in the presence of shot noise, a straight inversion becomes unstable leading to inaccurate estimation of the real-space harmonics. This problem can be overcome by Wiener filtering.

[5] The coupling matrix has a more complicated dependence on l and m for catalogues with incomplete sky coverage. Zaroubi & Hoffman (1996) derived a similar expression for the coupling matrix in Cartesian coordinates.

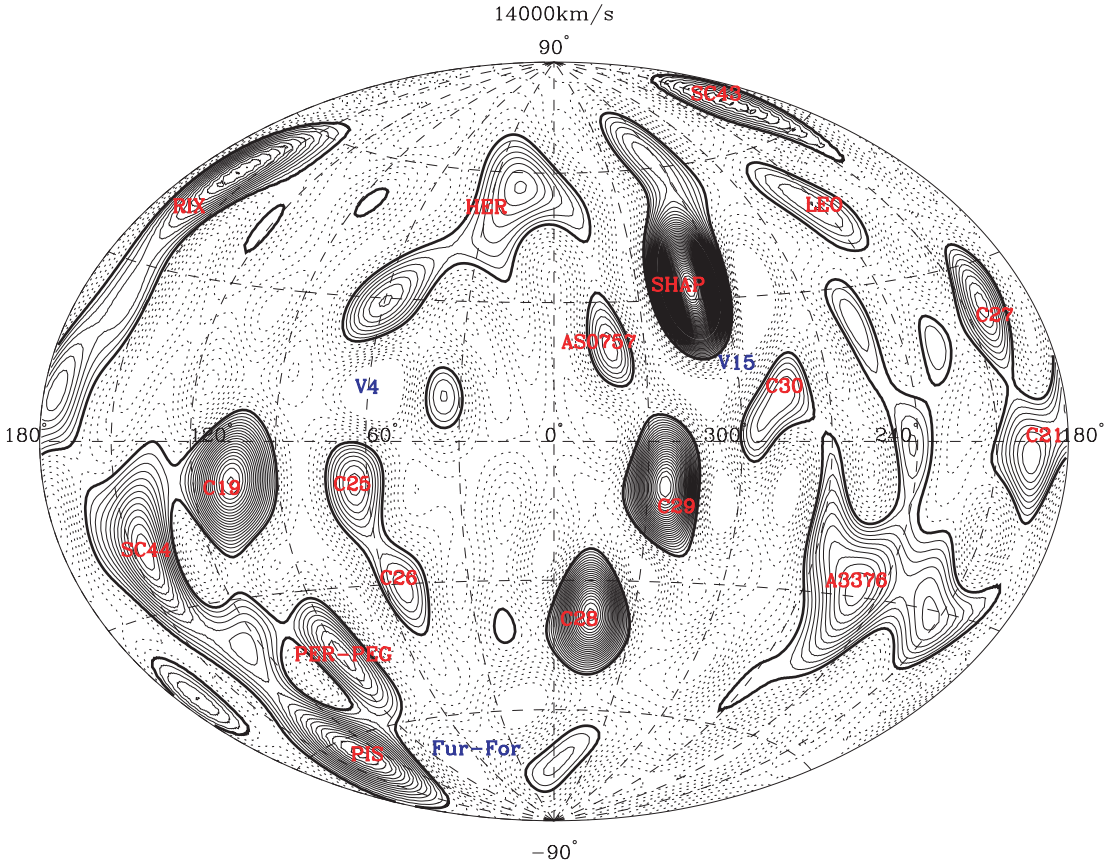

Figure 9. Same as in Fig. 3 but evaluated at 14 000 km s^{-1}. The overdensities are Rixos F231_526 (RIX), SC44, C19, Pisces (Pis), Perseus–Pegasus (Per–Peg), C25, C26, Hercules (Her), Abell S0757, C28, Shapley (Shap), C29, C30, SC 43, Leo, Abell 3376, C27 and C21. The voids are V4, Further–Fornax (Fur–For) and V15.

5 WIENER RECONSTRUCTION

In this section, we give the formulae for the Wiener filter method. For a full derivation, we refer the reader to Zaroubi et al. (1995) and Erdoğdu et al. (2004).

5.1 Model signal and noise matrices

For this analysis, the Wiener-filter reconstructed real-space density field is given by

$$\left(\delta^R_{lmn}\right)_{\rm WF} = \sum_{n'n''} \left(\mathbf{S}_l \left[\mathbf{S}_l + \mathbf{N}_l\right]^{-1}\right)_{nn'} \left(\mathbf{Z}_l^{-1}\right)_{n'n''} \delta^S_{lmn''}. \quad (12)$$

For the case $w(r) = 1/\phi_{\rm s}(r)$, the signal and noise matrices simplify to

$$(\mathbf{S}_l)_{nn'} \simeq P(k_n) C^{-1}_{ln} \delta^K_{nn'} \text{ and} \quad (13)$$

$$(\mathbf{N}_l)_{nn'} = \frac{1}{\bar{\rho}} \int_0^R {\rm d}r r^2 \frac{1}{\phi_{\rm s}(r)} j_l(k_n r) j_l(k_{n'} r), \quad (14)$$

respectively.

The expected scatter in the reconstructed density, $\langle \Delta\delta(\boldsymbol{r})\rangle^2$, is given by

$$\langle \Delta\delta(\boldsymbol{r})\rangle^2 = \frac{1}{4\pi} \sum_{lnn'} (2l+1)[(\mathbf{I} - \mathbf{F}_l)\mathbf{S}_l]_{nn'} \times C_{ln} C_{ln'} j_l(k_n r) j_l(k_{n'} r). \quad (15)$$

The scatter in the reconstructed radial velocity $\langle \Delta v_{\rm r}(\boldsymbol{r})\rangle^2$ fields can also be formulated in Fourier–Bessel space in an analogous way (cf. FLHLZ, appendix F):

$$\langle \Delta v_{\rm r}(\boldsymbol{r})\rangle^2 = \frac{H_0 \beta^2}{4\pi} \sum_{lnn'} (2l+1)[(\mathbf{I} - \mathbf{F}_l)\mathbf{S}_l]_{nn'} \times C_{ln} C_{ln'} \frac{j_l'(k_n r) j_l'(k_{n'} r)}{k_n k_{n'}}. \quad (16)$$

5.2 Choice of reference frame

The redshift distortion matrix given in Section 4 takes into account the motion of the observer, $\boldsymbol{v}(\mathbf{0})$, and thus the choice of reference frame is arbitrary. On the other hand, the formulation of $(\mathbf{Z}_l)_{nn'}$ involves the Taylor expansion of the velocity field out to first order in $\Delta\boldsymbol{v} = \boldsymbol{v}(\boldsymbol{r}) - \boldsymbol{v}(\mathbf{0})$ (see appendix D of FLHLZ). As such, the reconstruction will be more accurate in the frame in which $\Delta\boldsymbol{v}$ is smaller. Nearby where the galaxies share the LG motion, it is more accurate to correct for the redshift distortions in the LG frame. At larger distances, galaxy motions are independent of the LG velocity and thus $\Delta\boldsymbol{v}$ is smaller in the cosmic microwave background (CMB) frame. Since 2MRS probes the local universe ($cz_{\rm med} \approx 6000$ km s^{-1}), we will work with the LG frame redshifts. We will present the dipole velocity results from redshifts in both frames.

The choice of frame for the redshifts will not affect the frame of the reconstructed density field. In both cases, the reconstructed harmonics will be in real space. Consequently, the reconstructed velocity field (equation 9) will be in the CMB frame. It is possible

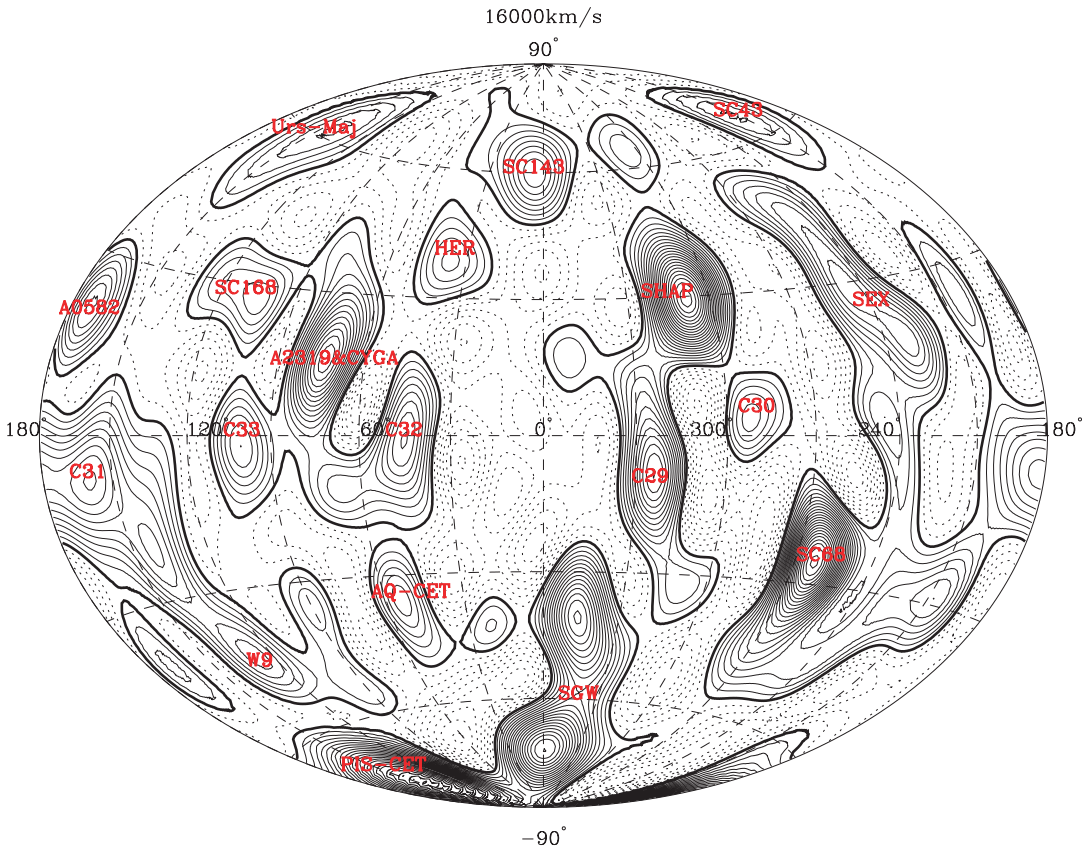

Figure 10. Same as in Fig. 3 but evaluated at 16 000 km s^{-1}. The overdensities are Abell 582, C31, Ursa Major (Urs Maj), SC168, West 9 (W9), C33, Abell 2319 & Cygnus A (CYGA), Pisces–Cetus (Pis–Cet), C32, Aquarius–Cetus (Aq–Cet), Hercules (Her), SC143, Southern Great Wall (SGW), C29, Shapley (Shap), C30, SC43, Sextans (Sex) and SC68.

to convert the velocity field into the LG frame by subtracting the LG velocity ($v_{\rm LG} = 627 \pm 22$ km s^{-1}, towards $l_{\rm LG} = 273^\circ \pm 3^\circ$, $b_{\rm LG} = 29^\circ \pm 3^\circ$; Courteau & Van Den Bergh 1999 and Bennett et al. 2003). In the following section, the reconstructed velocity maps will be presented in either the LG or the CMB frames. Up to 8000 km s^{-1} (Figs 11–14), it is difficult to see the real nature of the structures in the LG frame as the LG velocity dominates. Therefore, the maps will be plotted in the CMB frame. On larger distances (Figs 15–18), galaxies have positive CMB radial velocities so it is easier to compare the velocities in the LG frame than in the CMB frame.

6 APPLICATION TO THE 2MRS

The formalism discussed in the previous sections is limited to 4π sky coverage. In principle, the analysis can be extended to account explicitly for incomplete sky coverage. In this paper, a simpler approach has been adopted to fill in the galaxies masked by the Galactic Plane (the zone of avoidance). The masked area is divided into 36 bins of 10° in longitude. In each angular bin, the distance is divided into bins of $10\,h^{-1}$ Mpc. The galaxies in each longitude/distance bin are then sampled from the corresponding longitude/distance bins in the adjacent strips $-|b_{\rm masked}| - 10^\circ < b < |b_{\rm masked}| + 10^\circ$ (where $|b_{\rm masked}| = 5^\circ$ or $|b_{\rm masked}| = 10^\circ$). These galaxies are then placed in random latitudes within the mask region. The number of galaxies in each masked bin is set to a random Poisson deviate whose mean equals the mean number of galaxies in the adjacent unmasked strips. This procedure is carried out to mimic the shot noise effects. The success of this interpolation method depends on the interplay between the width of the mask, the angular resolution and whether the structure in the adjacent regions physically correlates with the structure in the zone of avoidance. The method is less robust for masked areas larger than $|b| = 15^\circ$ (Lahav et al. 1994). The width of the 2MRS mask is much smaller than this value and the survey penetrates deep into the zone of avoidance apart from very obscured regions near the centre of the Milky Way. We also test the effects of our method by varying the bin sizes and by filling the region uniformly instead of interpolating. We calculate the angular power spectrum for each case and find good agreement (Rassat et al., in preparation)between them.

The density field is expanded within a spherical volume of radius $R_{\rm max} = 20\,000$ km s^{-1}. We impose the condition that the density field outside $R_{\rm max}$ is zero and the logarithmic derivative of the gravitational potential is continuous at the boundary [which holds if $j_{l-1}(k_n R) = 0$ for all l]. There are two other possible boundary conditions discussed in FLHLZ: setting only the density or the radial velocity zero at the boundary. We have tested our reconstructions using these boundary conditions. Setting the density to zero at the boundary results in a discontinuous potential and the reconstructed radial velocities become unrealistically high. Up to a distance of 10 000 km s^{-1}, the fields reconstructed using the zero velocity boundary condition agree reasonably well with those reconstructed using the continuous potential condition; however, the radial velocities of the zero velocity reconstructions are slightly higher. Beyond 10 000 km s^{-1}, the radial velocities of the zero velocity reconstructions tend to zero; however, the backside infall into the Shapley Supercluster still exists.

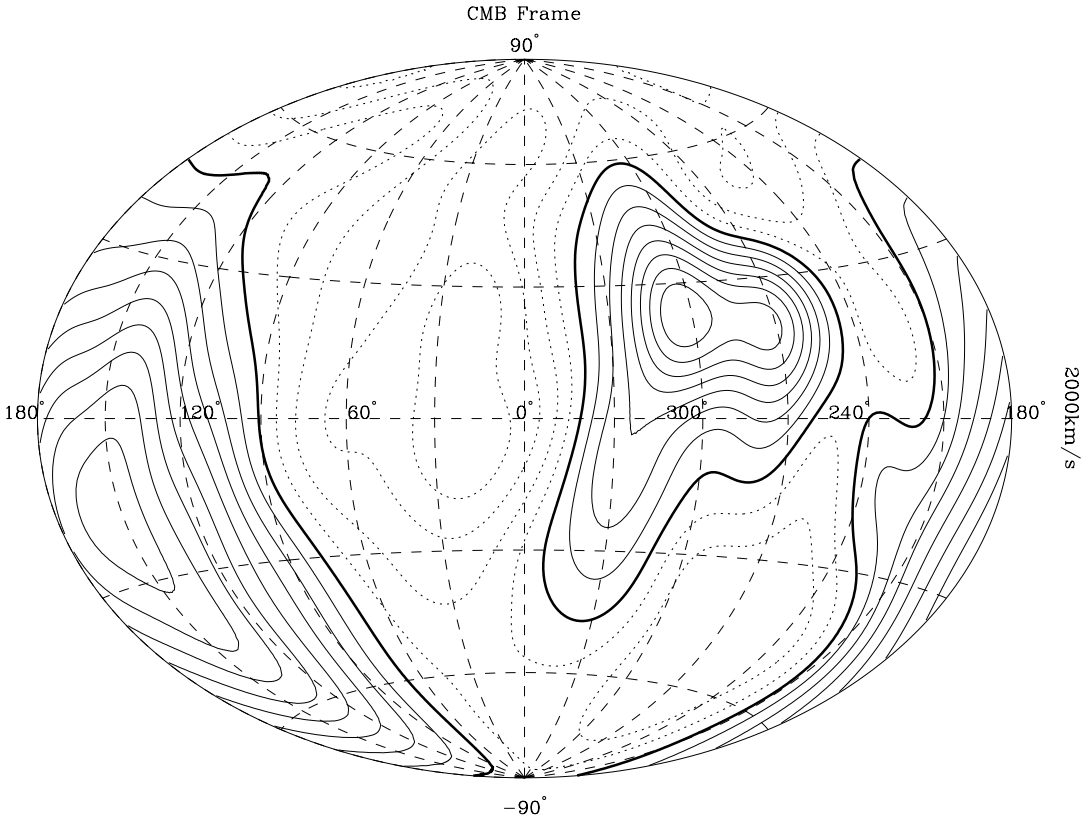

Figure 11. The reconstructed radial velocity field, evaluated on a thin shell at 2000 km s^{-1}, shown in Galactic Aitoff projection in the CMB frame. This velocity field corresponds with the density field shown in Fig. 3. Dashed lines show infall, and solid lines show outflow. The first solid line is for $v_{\rm radial} = 0\,{\rm km\,s^{-1}}$, and contour spacing is $|\Delta v_{\rm radial}| = 50\,{\rm km\,s^{-1}}$. Note the strong outflow towards the Great Attractor and flow out of the Local Void. Also Perseus–Pisces and N1600, cause an outflow towards ($l \simeq 165^\circ$, $b \simeq -30^\circ$).

Thus we conclude that setting the logarithmic derivative of the gravitational potential to be continuous at the boundary allows for a *smooth* transition of the density and velocity fields from $r < R_{\rm max}$ to $r > R_{\rm max}$ and as such gives the most robust results. We also note that FLHLZ, WLF and Schmoldt et al. (1999) use the same boundary condition for their reconstructions.

The resolution of the reconstruction depends on the maximum values of angular and radial modes (see fig. 6 of WLF). We want to have as high a resolution as possible without introducing artificial structures to the field. Therefore, we compute the harmonics up to $l_{\rm max} = 15$ angularly and $k_n R \leqslant 100$ radially. $l_{\rm max} = 15$ is chosen so that the angular resolution ($\delta\theta \sim \pi/l$) is comparable to the width of the interpolated region and the radial modes are chosen to match the angular resolution (see FLHLZ, appendix B for a detailed discussion).

The Wiener filter method requires a model for the linear galaxy power spectrum in redshift space, which depends on the real-space power spectrum and on the redshift distortion parameter, $\beta \equiv {\Omega_{\rm m}}^{0.6}/b$. The real-space power spectrum is well described by a scale-invariant cold dark matter (CDM) power spectrum with shape parameter $\Gamma \approx \Omega_{\rm m} h$, for the scales concerned in this analysis. The combined analysis of third year data from the *Wilkinson Microwave Anisotropy Probe* (*WMAP*; Spergel et al. 2006), the two-degree Field Galaxy Redshift Survey (2dFGRS; Cole et al. 2005) and the Sloan Digital Sky Survey (SDSS; Tegmark et al. 2004) imply $\Gamma \approx 0.17$. On the other hand, Frith, Outram & Shanks (2005) and Maller et al. (2005) analyse the angular power spectrum of the 2MASS galaxies and derive lower Γ values of 0.14 ± 0.02 and 0.116 ± 0.009, respectively. The normalization of the power spectrum is conventionally expressed in terms of the variance of the mass density field in spheres of $8\,h^{-1}$ Mpc, σ_8. Recent *WMAP* results combined with the 2dFGRS gives $\sigma_8 \approx 0.75$, whereas analysis of the 2MASS galaxies suggest $\sigma_8 \approx 0.9$ (Frith et al. 2005; Maller et al. 2005; Pike & Hudson 2005). In a previous paper, we analysed the 2MRS LG dipole and derived a value for β for 2MRS: $\beta = 0.4 \pm 0.09$ (Erdoğdu et al. 2006).

In order to check the goodness of fit of these different parameters to the data, we calculate the χ^2 statistic defined by

$$\chi^2 = \mathbf{d}^\dagger (\mathbf{S} + \mathbf{N})^{-1} \mathbf{d}, \tag{17}$$

for $\Gamma = (0.1, 0.2)$, $\sigma_8 = (0.7, 0.9)$ and $\beta = (0.3, 0.4, 0.5)$. Changing Γ does not affect the χ^2 values greatly but $\Gamma = 0.2$ is a slightly better fit. Varying σ_8 is a bit more influential on the χ^2 values; however, the reconstructed maps look very similar for these models. Increasing Γ decreases the power on large scales and, therefore, the peculiar velocities tend to be smaller but the difference is negligible. Decreasing σ_8 has the same effect on the power spectrum as increasing Γ. The choice of β plays a more important role in the goodness-of-fit results but has little effect on the reconstructed maps other than a linear scaling of peculiar velocities. In the analysis that follows, we adopt $\Gamma = 0.2$, $\sigma_8 = 0.7$ and $\beta = 0.5$, which is the best-fitting model that was considered, with a reduced χ^2 value of 1.3. We note that the best-fitting β is higher than derived in Erdoğdu et al. (2006), this discrepancy will be discussed in Section 6.3. In a forthcoming paper (Rassat et al., in preparation), we will present a detailed analysis of the cosmological parameters of 2MRS.

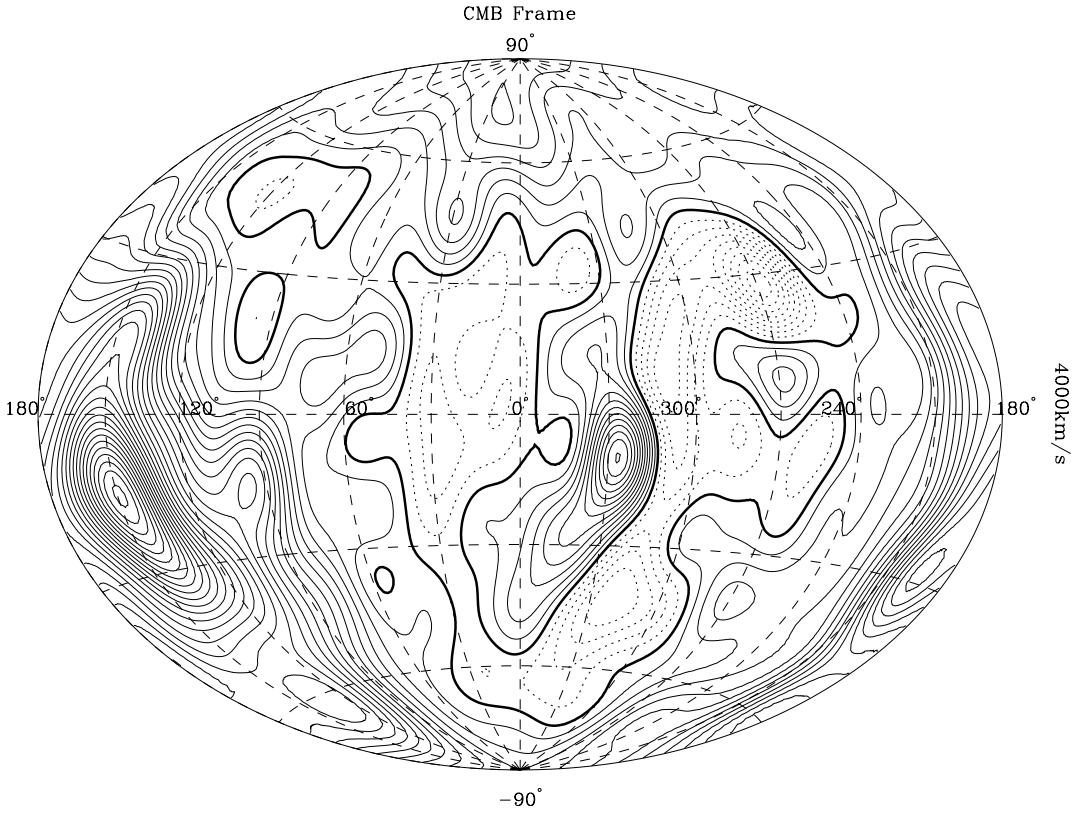

Figure 12. Same as Fig. 11 but evaluated at 4000 km s^{-1}. This velocity field corresponds with the density field shown in Fig. 4. Note that Perseus–Pisces and N1600 cause the strongest outflow towards ($l \simeq 150°$, $b \simeq -20°$). There is also a flow towards the centre of Pavo–Indus–Telescopium ($l \simeq 335°$, $b \simeq -25°$) and a weaker one towards Hydra ($l \simeq 280°$, $b \simeq 10°$).

6.1 Density maps

Figs 3–10 show the Aitoff projections of the reconstructed density field in real space, plotted in Galactic coordinates, evaluated at different distance slices.

Fig. 3 shows a thin density shell at $r = 2000$ km s^{-1}. The expected scatter in the reconstructed density field is $\langle \Delta\delta(\boldsymbol{r}) \rangle = 0.31$ and this value stays approximately the same out to $r = 10\,000$ km s^{-1} and increases by 0.1 thereafter. All the known structures are resolved and the field at this distance is dominated by interconnecting voids. The Puppis cluster (Lahav et al. 1993; S1 in Saunders et al. 1991) is very prominent and extends down to $b \simeq -28°$. The overdensity labelled as C1 ($l \simeq 190°$, $b \simeq 5°$) does not correspond to any previously observed structure.

Fig. 4 is the 2MRS density field at $r = 4000$ km s^{-1}. Hydra ($l \simeq 270°$, $b \simeq 50°$) and Centaurus ($l \simeq 300°$, $b \simeq 20°$) continue in this shell but now are separated by the Hydra void. Centaurus is connected to the new overdensities C2 ($l \simeq 345°$, $b \simeq 10°$) and C8 ($l \simeq 295°$, $b \simeq 7°$) and Hydra connects to C4 ($l \simeq 240°$, $b \simeq 25°$). Pavo–Indus–Telescopium continues deep into the zone of avoidance and connects to the Centaurus Wall as suggested by Fairall (1988). The well-known cluster Cancer ($l \simeq 210°$, $b \simeq 30°$), as well as new clusters C3 ($l \simeq 275°$, $b \simeq -30°$), C5 ($l \simeq 195°$, $b \simeq 0°$), C6 ($l \simeq 170°$, $b \simeq -15°$) and C7 ($l \simeq 55°$, $b \simeq 15°$), all peak at $r = 5000$ km s^{-1} with C5, C6 and C7 connecting to Pegasus and the Perseus–Pisces Wall. The overdensity Cϵ (WLF) is more prominent in the 2MRS field than in *IRAS* 1.2-Jy field. The Perseus and Pisces clusters are picked up as two distinct overdensities and both connect to Camelopardalis ($l \simeq 145°$, $b \simeq 30°$) and Cetus ($l \simeq 190°$, $b \simeq -55°$) at $r = 5000$ km s^{-1}.

Fig. 5 is the density field at $r = 6000$ km s^{-1}. Hydra ($l \simeq 285°$, $b \simeq 5°$) is less prominent in this shell whereas Pavo–Indus–Telescopium ($l \simeq 0°$, $b \simeq -45°$) is still strong. The cluster Abell 3627 (or Norma, $l \simeq 330°$, $b \simeq -10°$) which was recognized as the centre of the Great Attractor[6] by Kraan-Korteweg et al. (1996), peaks around $r = 5000$ km s^{-1} and is separated from the Centaurus Wall by the Sculptor Void. The overdensity labelled as C8 continues from the previous shell and contains the luminous CIZA J1324.7−5736, cluster which was discovered by Ebeling, Mullis & Tully (2002) and the Centaurus–Crux cluster (Woudt 1998). The Abell clusters 569 ($l \simeq 155°$, $b \simeq -15°$) and 168 ($l \simeq 120°$, $b \simeq 70°$) are as prominent as the Perseus–Pisces ridge and both are connected to it. The clusters labelled as WLB (e.g. WLB 248 at $l \simeq 240°$, $b \simeq 40°$) were identified by White et al. (1999). There are two previously unidentified voids at this distance labelled as V1 and V2 and a cluster at ($l \simeq 240°$, $b \simeq 8°$) labelled C9.

Fig. 6 is the 2MRS density field at $r = 8000$ km s^{-1}. The Great Wall (Geller & Huchra 1989) connects to the Ophiuchus supercluster discovered by Wakamatsu et al. (1994). The massive Shapley supercluster is already visible ($l \simeq 300°$, $b \simeq 30°$) at this distance. The void V1 continues to this shell. The new clusters C10 ($l \simeq 205°$, $b \simeq 10°$), C11 ($l \simeq 250°$, $b \simeq -10°$), C12 ($l \simeq 325°$, $b \simeq -10°$) and C13 ($l \simeq 85°$, $b \simeq 13°$) lie on galactic latitudes. The cluster ZwCl 0943.7+5454 was first identified by Zwicky & Herzog (1966) and K42 by Klemola (1969). All the superclusters labelled as SC (e.g. SC 129 in this shell) are given in Einasto et al. (1997, table 2)

[6] By 'Great Attractor', it is meant the entire steradian on the sky centred at ($l \sim 310°$, $b \sim 20°$) covering a distance of 20 h^{-1} Mpc to 60 h^{-1} Mpc.

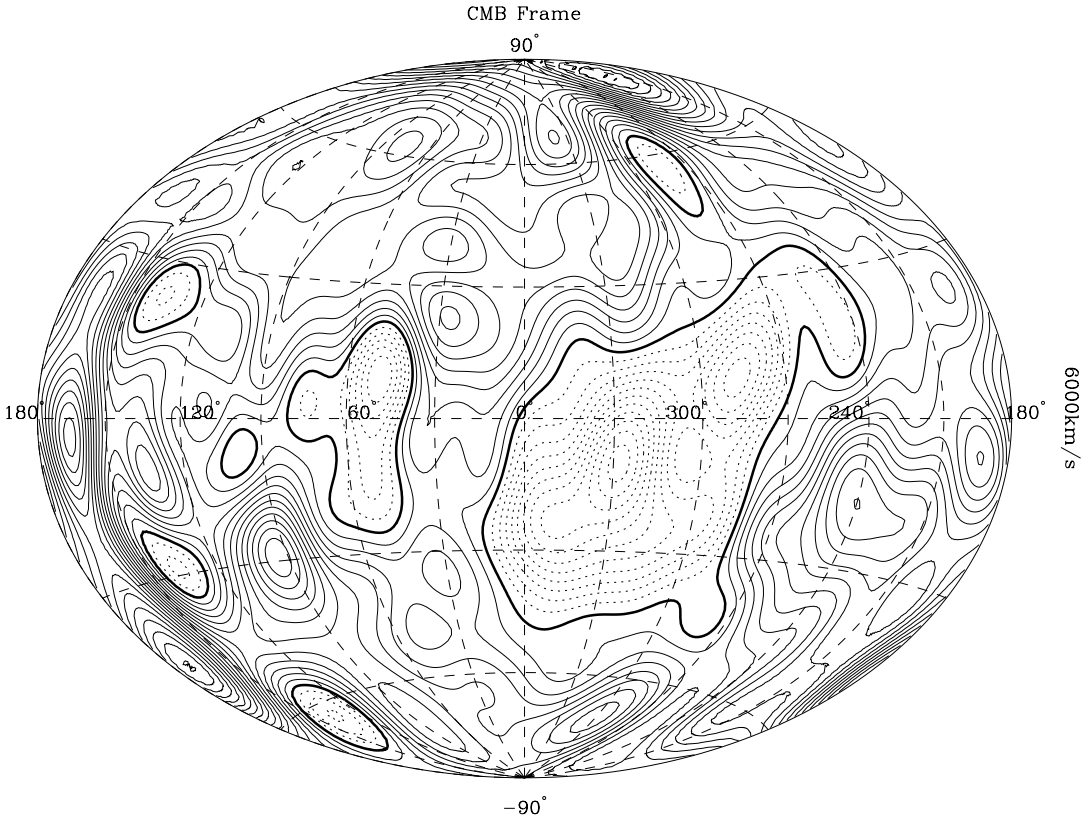

Figure 13. Same as Fig. 11 but evaluated at 6000 km s^{-1}. This velocity field corresponds with the density field shown in Fig. 5. Note the strong outflow towards the Great Wall, especially towards Coma and the general velocity flow towards the North Galactic Pole from the South Galactic Pole. There is still some outflow towards Pegasus. Also visible is a strong backside infall towards the Great Attractor region and Perseus–Pisces.

and structures labelled CAN and CID (e.g. CAN 136 in this shell and CID 15 in the next shell) are clusters given in Wegner et al. (1999).

Fig. 7 is the 2MRS density field at $r = 10\,000$ km s^{-1}. The expected scatter now rises to $\langle \Delta\delta(\boldsymbol{r})\rangle = 0.36$. The mighty Hercules supercluster dominates this shell and Shapley begins to appear. Other dominant structures are CID (CAN) 15 and 16.

Fig. 8 is the 2MRS density field at $r = 12\,000$ km s^{-1} and has a scatter of $\langle \Delta\delta(\boldsymbol{r})\rangle = 0.41$. The Perseus–Pegasus and Pisces (Einasto et al. 1997) superclusters, C20 and Abell 576 continue the Perseus–Pisces wall and dominate the shell.

Fig. 9 is the 2MRS density field at $r = 14\,000$ km s^{-1} with scatter $\langle \Delta\delta(\boldsymbol{r})\rangle = 0.46$. The density field of the Shapley supercluster peaks at this distance and connects to C28 and C29 at $r = 15\,000$ km s^{-1} to form a ridge.

Fig. 10 is the 2MRS density field at $r = 16\,000$ km s^{-1}. The expected scatter is $\langle \Delta\delta(\boldsymbol{r})\rangle = 0.49$. The most conspicuous structure is the Pisces-Cetus supercluster, which connects to the Southern Great Wall. The Perseus–Cetus also dominates the southern strips of the 2dF (see e.g. Erdoğdu et al. 2004; Porter & Raychaudhury 2005) and Sloan surveys (e.g. Porter & Raychaudhury 2005). We note that at this distance, we do not pick up any voids. This is due to the nature of our technique. The Wiener filter method will predict the mean field in the absence of data. Since the density field is constructed to have zero mean, the Wiener filter signal will approach to zero at the edges of the survey where the shot noise dominates. This leads to the signal being reconstructed in a non-uniform manner. As such, we do not present maps of the density and velocity fields beyond 16 000 km s^{-1} after which the shot noise is too high and the Wiener-filtered fields tend to zero.

6.2 Velocity maps

Figs 11–18 show the Galactic Aitoff projections of the radial velocity fields for $\beta = 0.5$ evaluated across the same shells as the density fields shown in Figs 3–10. Positive (outflowing) radial velocities are shown as solid lines and the negative (infalling) radial velocities are shown as dashed lines. The contour spacing is $|\Delta v_{\rm radial}| = 50$ km s^{-1}.

Figs 11 and 12 show the CMB frame radial velocity fields at $r = 2000$ km s^{-1} and at $r = 4000$ km s^{-1}, respectively. The expected scatter in the velocity field is $\langle \Delta \boldsymbol{v}\,(\boldsymbol{r})\rangle = 53$ km s^{-1} at $r = 2000$ km s^{-1} and $\langle \Delta \boldsymbol{v}\,(\boldsymbol{r})\rangle = 62$ km s^{-1} at $r = 4000$ km s^{-1}. At $r = 2000$ km s^{-1}, there is a strong outflow towards the Virgo Great Attractor ($l \simeq 290^\circ$, $b \simeq 15^\circ$) and inflow out of the underdense regions. Also seen at this distances are the effects of Perseus–Pisces and N1600, causing a strong outflow towards ($l \simeq 165^\circ$, $b \simeq -30^\circ$). At $r = 4000$ km s^{-1}, Perseus–Pisces and N1600 are the dominant structures causing an outflow towards ($l \simeq 150^\circ$, $b \simeq -20^\circ$). There is also a flow towards the centre of Pavo–Indus–Telescopium ($l \simeq 335^\circ$, $b \simeq -25^\circ$) and a backside infall to Hydra. The backside infall to the Great Attractor region becomes strongest at $r = 5000$ km s^{-1} and reaches to $v_{\rm infall} = (982 \pm 400)\beta$ km s^{-1} in the LG frame and $v_{\rm infall} = (127 \pm 409)$ β km s^{-1} in the CMB frame, where the quoted values are the mean of the velocity field around the region and the error bars are the standard deviation from that mean and the expected scatter in the velocity field added in quadrature.

Although still visible at $r = 4000$ km s^{-1}, the Great Wall really starts to dominate in Fig. 13 at a distance of $r = 6000$ km s^{-1}. At this distance the velocity scatter rises to $\langle \Delta \boldsymbol{v}(\boldsymbol{r})\rangle = 72$ km s^{-1}. Here the fall towards the Coma Cluster is quite apparent at $l \simeq 240^\circ$ and

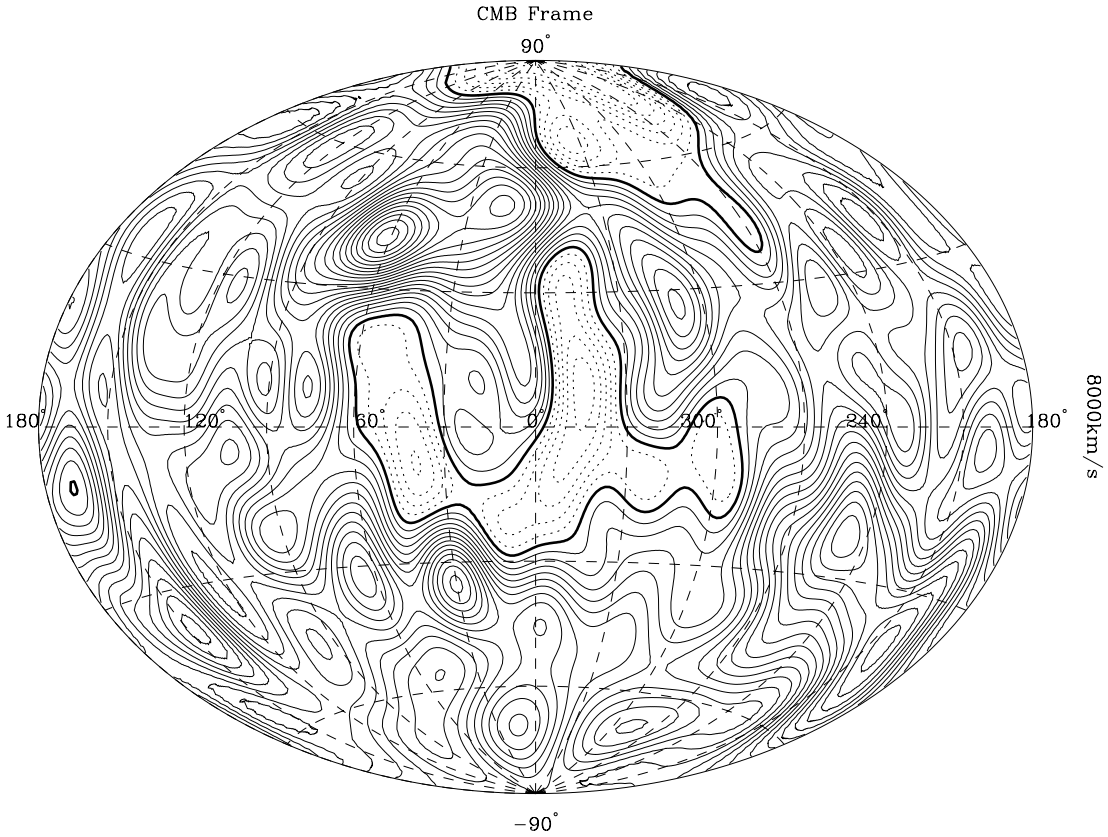

Figure 14. Same as Fig. 11 but evaluated at 8000 km s^{-1}. This velocity field corresponds with the density field shown in Fig. 5. There is still a strong outflow towards the clusters of the Great Wall. The outflow towards Shapley ($l \simeq 310^\circ$, $b \simeq 25^\circ$) is already visible. The Sculptor Wall is implied in the outflow towards the Southern Galactic Pole.

$b \simeq 80^\circ$. The velocity flow towards Perseus–Pisces is still strong and there is some outflow towards Pegasus ($l \simeq 95^\circ$, $b \simeq -60^\circ$), Phoenix ($l \simeq 330^\circ$, $b \simeq -75^\circ$), the Abell clusters A548, A539 ($l \simeq 230^\circ$, $b \simeq -20^\circ$) and A400 ($l \simeq 175^\circ$, $b \simeq -45^\circ$). The CMB radial velocities at $r = 8000\,\mathrm{km\,s^{-1}}$, shown in Fig. 14, have scatter of $\langle \Delta \boldsymbol{v}\,(\boldsymbol{r})\rangle = 87\,\mathrm{km\,s^{-1}}$ and are mostly outflowing apart from the remnants of backside infall towards the Great Attractor and the Coma cluster. By $r = 10\,000\,\mathrm{km\,s^{-1}}$, it becomes difficult to compare peculiar velocities in the CMB frame so we switch to the LG frame. At $r = 10\,000\,\mathrm{km\,s^{-1}}$ [Fig. 15; $\langle \Delta \boldsymbol{v}\,(\boldsymbol{r})\rangle = 108\,\mathrm{km\,s^{-1}}$], the dipole velocity of the LG is still visible; however, there is an outflow towards Shapley ($l \simeq 310^\circ$, $b \simeq 25^\circ$) and the Hercules supercluster ($l \simeq 20^\circ$, $b \simeq 45^\circ$). Shapley outflow becomes stronger at $r = 12\,000\,\mathrm{km\,s^{-1}}$ [Fig. 16; $\langle \Delta \boldsymbol{v}\,(\boldsymbol{r})\rangle = 130\,\mathrm{km\,s^{-1}}$], begins to decrease at $r = 14\,000\,\mathrm{km\,s^{-1}}$ [Fig. 17; $\langle \Delta \boldsymbol{v}\,(\boldsymbol{r})\rangle = 146\,\mathrm{km\,s^{-1}}$] and at $r = 16\,000\,\mathrm{km\,s^{-1}}$ [Fig. 18; $\langle \Delta \boldsymbol{v}\,(\boldsymbol{r})\rangle = 150\,\mathrm{km\,s^{-1}}$] there is a strong backside infall towards it.

Fig. 19 shows the 2MRS density and velocity fields in the Supergalactic plane (SGP) ($SGZ = 0\,\mathrm{km\,s^{-1}}$) in different reference frames. The top plot is the reconstructed three-dimensional peculiar velocity field in the CMB frame, superimposed on the reconstructed density field in the SGP. The bottom plot is the same as the one on the left but the superimposed peculiar velocity field is reconstructed in the LG frame (obtained by subtracting the LG velocity ($v_{\mathrm{LG}} = 627 \pm 22\,\mathrm{km\,s^{-1}}$, towards $l_{\mathrm{LG}} = 273^\circ \pm 3^\circ$, $b_{\mathrm{LG}} = 29^\circ \pm 3^\circ$). The extent of the planar density distribution in the SGP can clearly be seen in these plots. Since the LG is moving towards the Great Attractor/Shapley region, the strong outflow towards the positive y-plane seen in the top plot decreases in the bottom plot. For the same reason, the outflow towards the negative y-plane is much stronger in the LG frame (bottom plot) than in the CMB frame. The most intriguing result is the connectivity of the Shapley supercluster (SGX, SGY) = (−12 000, 7000) to the Great Attractor region. The Virgo cluster at (SGX, SGY) = (0, 1000) also appears connected to the Great Attractor. The Perseus–Pisces supercluster also is visible at (SGX, SGY) = (2500, −4500) and Camelopardalis is at (SGX, SGY) = (45, −30). The other visible superclusters are Columba at (SGX, SGY) = (7500, −11 000) and Hercules (SGX, SGY) = (−13 000, −4000). In both plots, the outflow is dominated by Shapley, particularly in the CMB frame. The flow towards Virgo and the Perseus–Pisces region is also apparent and the flow towards the Great Attractor is clearly visible. Also observed is a significant flow towards Columba and some towards Hercules. After 16 000 km s^{-1}, the shot noise is too high and the density field becomes non-uniform.

Over the past years, there has been some disagreement over the existence of backside infall towards the GA (e.g. Dressler & Faber 1990; Mathewson, Ford & Buchhorn 1992). We find a clear backside infall, visible in both plots and in particular the one in the LG frame. The highest velocity back-falling velocity around the GA region is $800 \pm 600\ \beta^{-1}\,\mathrm{km\,s^{-1}}$ (at $55\ h^{-1}$ Mpc) in the CMB frame. In Fig. 20, we plot the average radial velocity field in towards the centres of the GA ($290^\circ \leqslant l \leqslant 320^\circ$, $-25^\circ \leqslant b \leqslant 60^\circ$ $-25^\circ \leqslant b \leqslant 70^\circ$, $r \leqslant 80\,h^{-1}$ Mpc) and the Shapley ($290^\circ \leqslant l \leqslant 320^\circ$, $40^\circ \leqslant b \leqslant 70^\circ$, $r \geqslant 80\,h^{-1}$ Mpc) Superclusters as a function of distance. The red lines are for the LG frame and the black lines are for the CMB frame. The solid lines denote the mean of the reconstructed velocities and the dashed lines are the errors calculated from the standard deviation of velocities in that region and the expected velocity

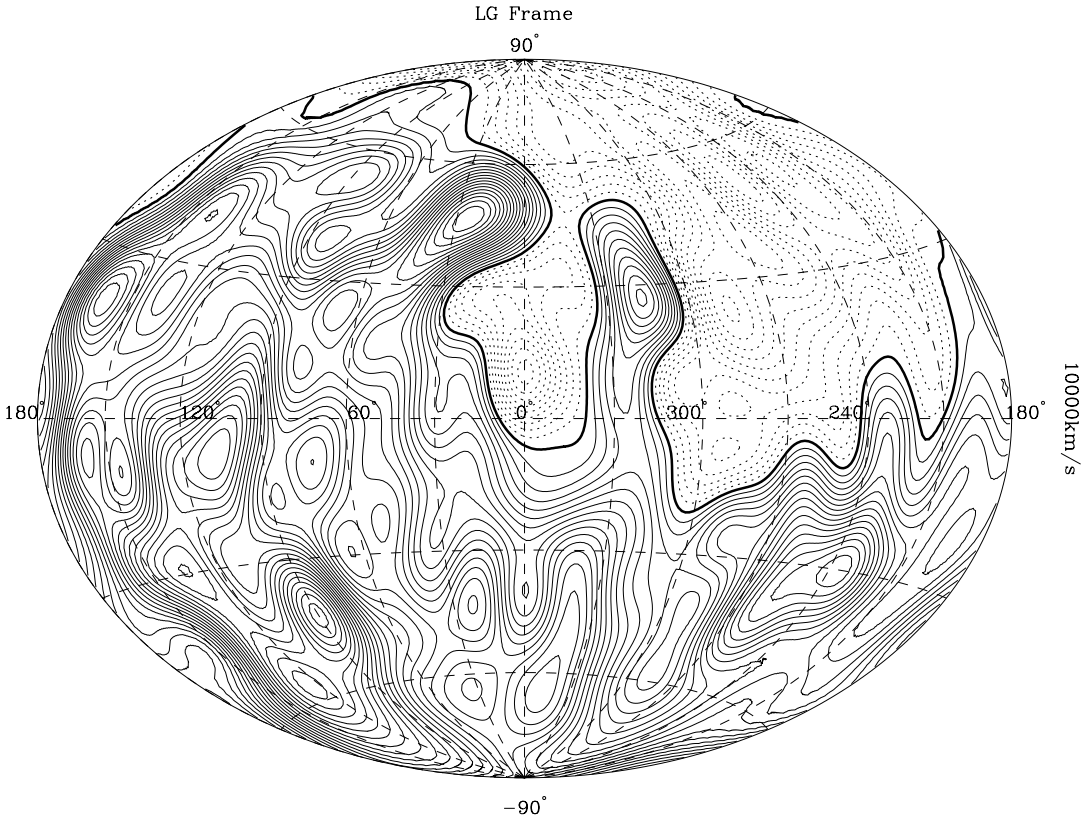

Figure 15. Same as Fig. 11 but evaluated at 10 000 km s^{-1} and in the LG frame instead of the CMB frame. There are three superclusters that dominate the outflow, Hercules towards ($l \simeq 20^\circ$, $b \simeq 45^\circ$), Shapley towards ($l \simeq 320^\circ$, $b \simeq 25^\circ$) and Columba towards ($l \simeq 225^\circ$, $b \simeq -30^\circ$).

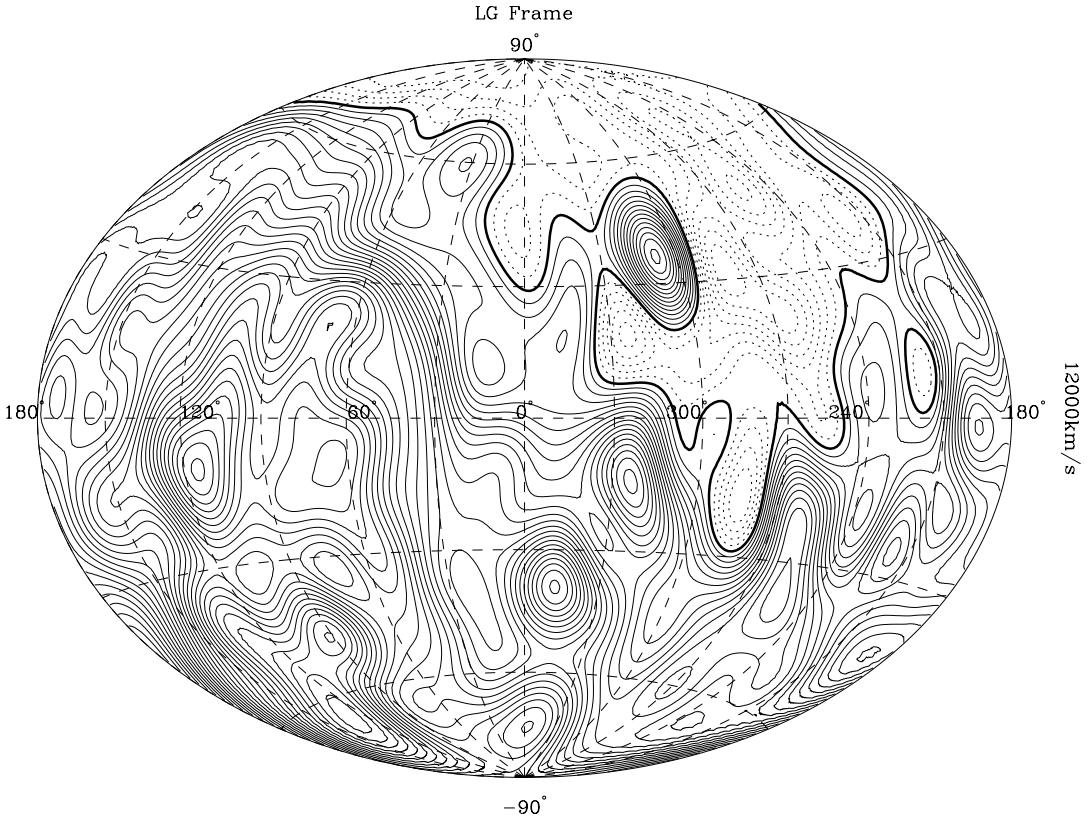

Figure 16. Same as Fig. 11 but evaluated at 12 000 km s^{-1} and in the LG frame instead of the CMB frame.

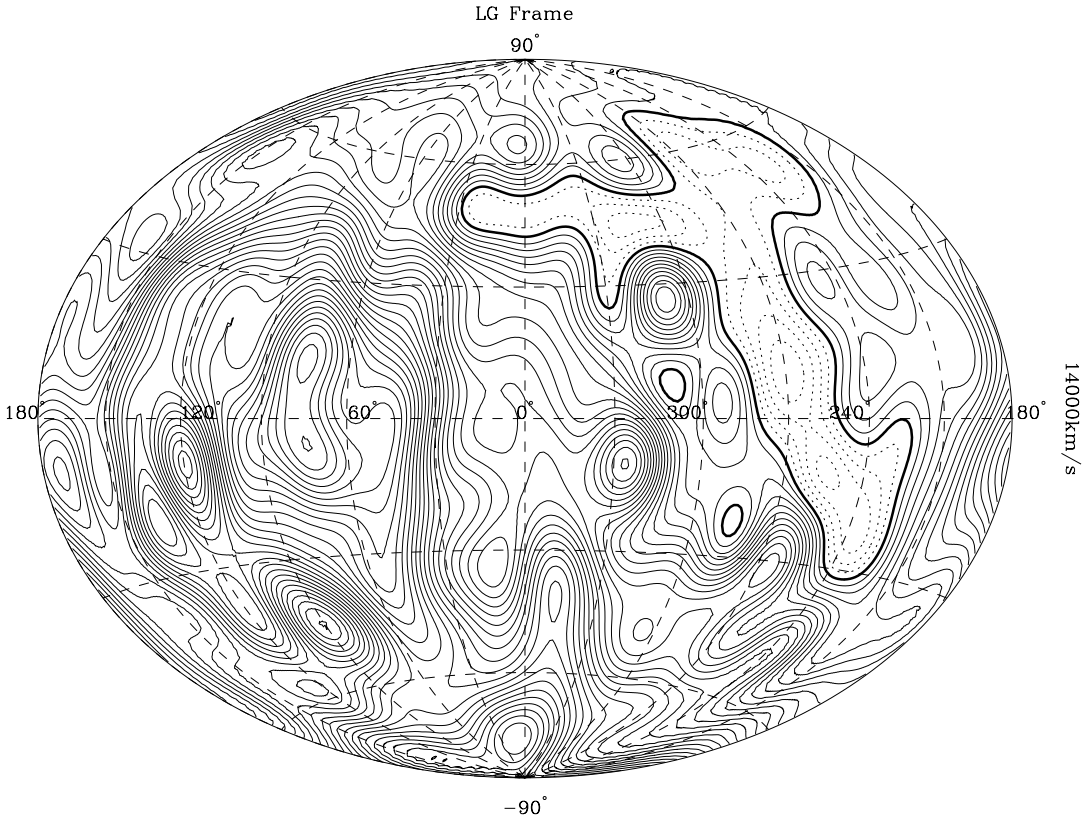

Figure 17. Same as Fig. 11 but evaluated at 14 000 km s^{-1} and in the LG frame instead of the CMB frame.

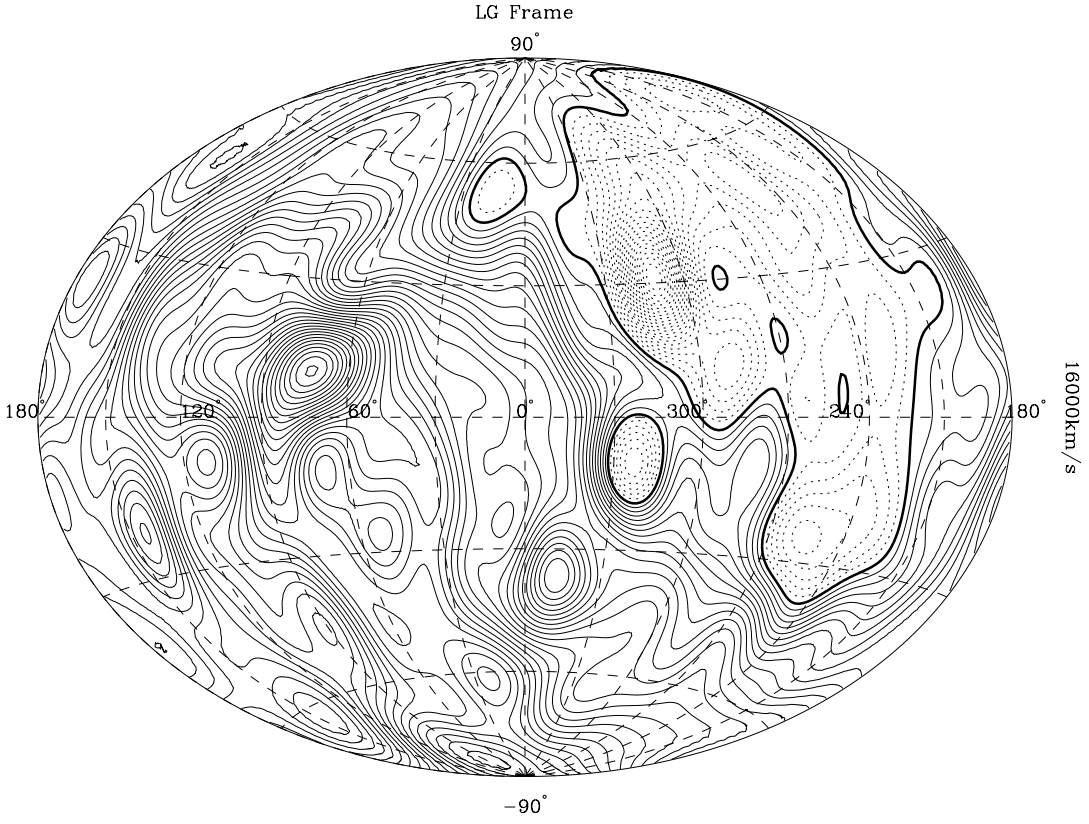

Figure 18. Same as Fig. 11 but evaluated at 16 000 km s^{-1} and in the LG frame instead of the CMB frame.

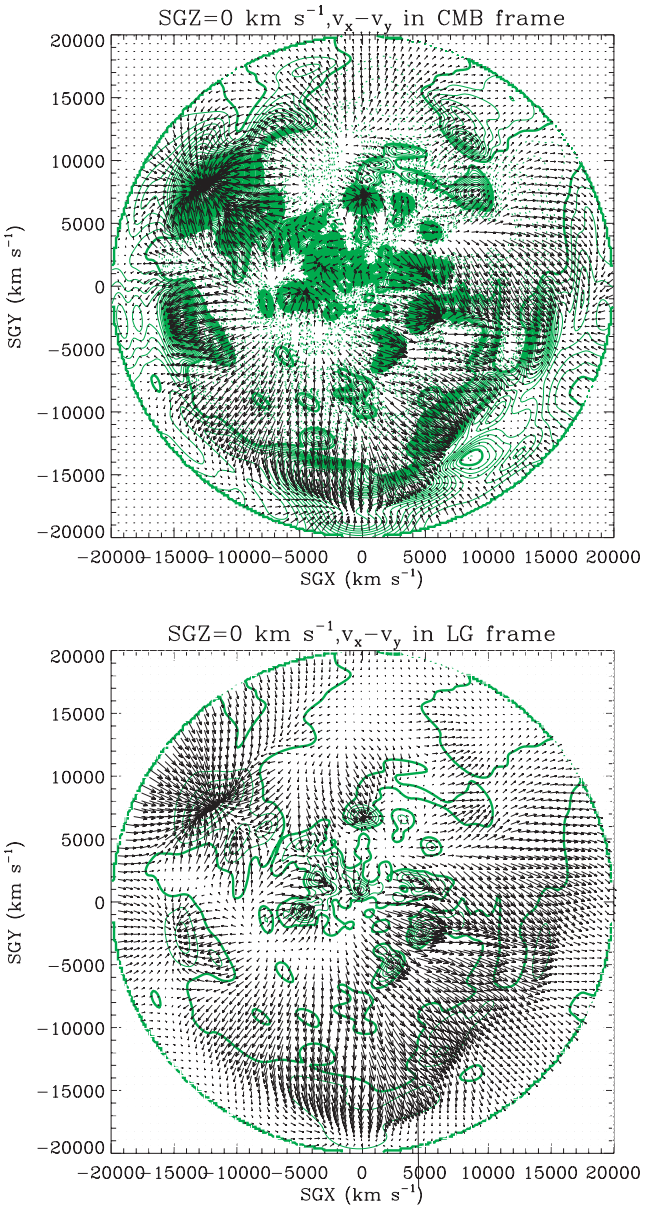

Figure 19. The reconstructed density fields in the SGP. The spacing of the density contours is $|\Delta\delta = 0.1|$ with dashed lines denoting the negative and the solid line denoting the positive density contrast. Superimposed in black are the reconstructed three-dimensional peculiar velocity field in the CMB (top plot) and the LG (bottom plot) frames. The length of the arrows are about 300 km s^{-1} per cell. The main overdensities are Hydra–Centaurus (centre left), Perseus–Pisces (centre right), Shapley Concentration (upper left), Coma (upper middle).

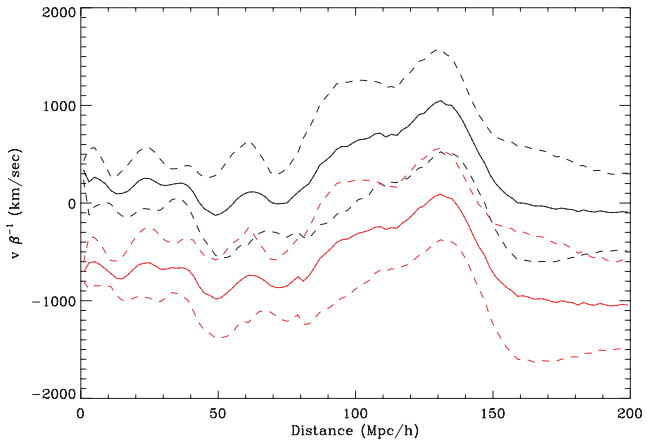

Figure 20. The radial velocity field in the region of the GA and the Shapley Superclusters as a function of distance. The red lines are for the LG and the black lines are for the CMB frame. The solid lines denote the mean of the reconstructed velocities and the dashed lines are the errors calculated from the standard deviation of velocities and the expected velocity scatter added in quadrature. The regions with negative velocities move towards us and positive velocities move away from us.

scatter added in quadrature. In this plot, the back infall on to the GA and the subsequent outflow towards Shapley are clearly visible. An observer in the GA would see the surrounding nearby galaxies moving towards her. On larger scales, she would observe a dipole velocity towards Shapley. If she was in the Shapley Supercluster (at $r \approx 130\,h^{-1}$ Mpc), she would observe that the surrounding galaxies are moving towards her. Whilst, this backside infall on to the GA was also observed by FLHLZ, WLF and Schmoldt et al. (1999), other authors who applied different reconstruction techniques to *IRAS* galaxy catalogues (e.g. Davis et al. 1996; Branchini et al. 1999; Valentine, Saunders & Taylor 2000) find little evidence of it.

Although the 2MRS sample is the densest all-sky sample to date and as such allows the most precise reconstruction of the local velocity field, our results are still not conclusive. In a forthcoming paper, we will compare the reconstructed fields with the observed velocity fields based on the distance measurements to elliptical galaxies in the 6dFGS and a new survey of spirals in the *I* band (SFI++) to assess the significance of this backside infall.

6.3 Alternative reconstruction methods

In order to assess the effects of the systematic errors of our method, we also carried out the reconstructions using alternative methods. Fig. 21 shows several of these reconstructions on the SGP out to 6000 km s^{-1}. The top left-hand plot is the unsmoothened harmonic reconstruction of the 2MRS density field in redshift space. It can clearly be seen that the harmonics are strongly affected by shot noise. Overdensities follow circular paths about the origin as a result of correlations introduced by noise. These artefacts are still clearly evident in the top right plot where the density field is corrected for redshift distortions (using equation 11) but without noise suppression. The correction of the redshift distortions reduces the overall amplitude of the density contrasts and makes the structures more spherical. This reconstruction corresponds to the unbiased minimal variance (umv) estimation of Zaroubi (2002) since in our case the redshift distortion matrix is invertible. The bottom left-hand panel shows the real-space density field after the Wiener Filter has been applied. As expected the Wiener Filter mitigates the effects of shot noise, removing the artefacts and high-frequency harmonics from the map; however, the Wiener-reconstructed field is biased towards the mean field which is zero by construction. In fact, the variance of the Wiener-filtered field is always smaller than the variance of the *true* underlying field. In order to overcome this drawback, Yahil (1994) introduced an alternative filter which preserves the power in the underlying field. This filter is defined as the square root of the Wiener filter. With this definition, the filtered field equals to that of the true field. The bottom right panel shows the real-space density field reconstructed using Yahil's filter. Whilst the estimated field is unbiased, the reconstruction is not optimal in the sense of

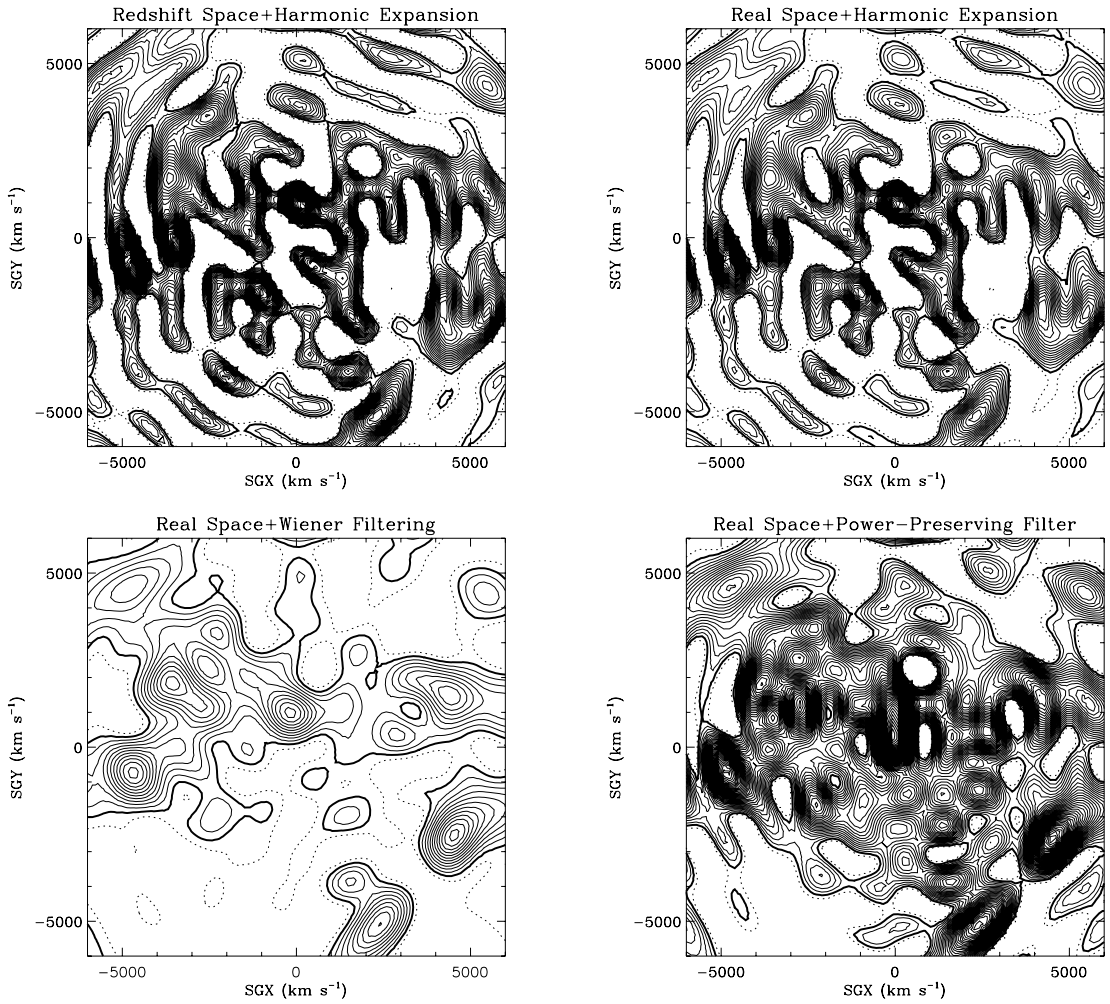

Figure 21. Reconstructions of the 2MRS density field in the SGP. All contours are spaced at $|\Delta\delta| = 0.5$, with solid (dashed) contours denoting positive (negative) contours. Top left-hand panel: the density field expanded in spherical harmonics with no smoothing. Top right-hand panel: same as in top left but with the harmonics corrected for redshift distortion. Bottom left-hand panel: same as in top right but smoothed by the Wiener filter. Bottom right-hand panel: the real-space density field smoothed by the power-preserving filter.

minimum variance and there are artefacts due to insufficient reduction of noise.

6.4 The acceleration of the LG

A detailed calculation of the acceleration of LG using the 2MRS data was given by Erdoğdu et al. (2006). In this section, the LG velocity is reconstructed from the density field. There are two main advantages of the analysis performed in this paper. First, working with spherical harmonic allows for reliable correction of the velocity flows and secondly, the Wiener filtering suppresses the noise self-consistently. The LG dipole is linear in the galaxy density field (assuming linear biasing). Consequently, the dipole computed from the Wiener filter algorithm will be an optimal (in the sense of minimum variance) estimate of the dipole due to matter within the reconstruction volume as long as non-linear effects can be neglected.

The reconstructed 2MRS dipole (equation 10) and the expected scatter (equation 16) in the reconstruction are plotted as a function of distance in the top plot of Fig. 22. The bottom plot of Fig. 22 shows the angle between the direction of the LG dipole and the CMB dipole ($l = 273^\circ$, $b = 29^\circ$). The black line is the dipole reconstructed with $\beta = 0.5$ (rescaled to $\beta = 1.0$) and the dashed line denotes the scatter in the velocity reconstruction. The inversion of the radial coupling matrix introduces a non-linear relationship between the value of β and the amplitude of the reconstructed acceleration. To illustrate this, we also plot the dipole reconstructed with $\beta = 1.0$ (the green line). The amplitudes of the dipole reconstructions using $\beta = 0.5$ and $\beta = 1.0$ are in good agreement (within the expected scatter) and the misalignment angles are almost the same up to 13 000 km s^{-1}. The blue line is the dipole reconstructed with $\beta = 0.5$ from the CMB redshifts. As expected, the amplitude of the dipole is underestimated at nearby distances and the misalignment angle is bigger than the dipole reconstructed from the LG redshifts. We conclude that, since the LG dipole is dominated by nearby galaxies, it is more accurate to use the LG redshifts in the reconstruction.

We also plot the number-weighted dipole obtained using raw redshifts (solid red line Erdoğdu et al. 2006) and the associated shot noise (dashed red line). The bottom plot indicates that the direction of the Wiener-reconstructed dipole is consistent with the dipole obtained in Erdoğdu et al. (2006). Both dipoles show the 'tug of war' between the Great Attractor and Perseus–Pisces and the dipole velocities are dominated by structure within the distance of

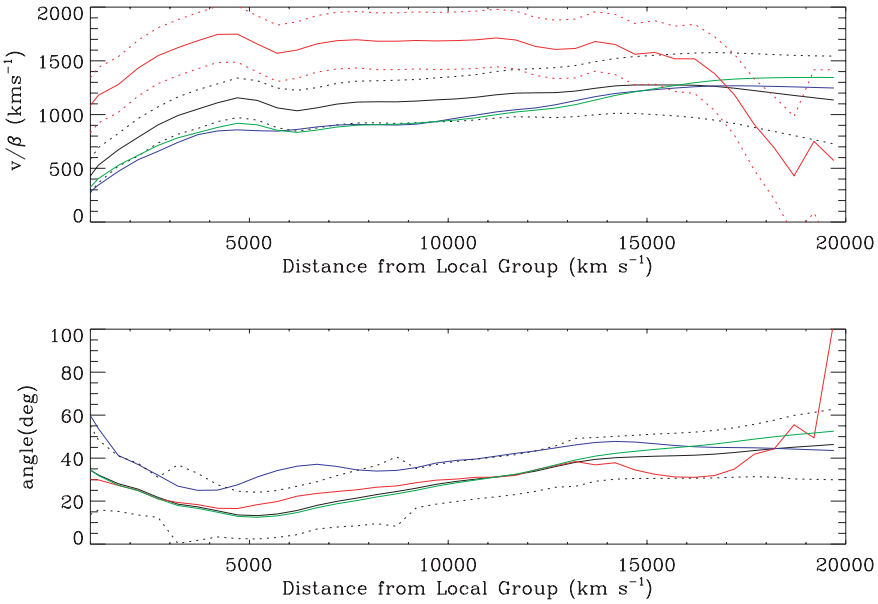

Figure 22. Top plot: the growth of acceleration of the LG due to galaxies within a series of successively larger concentric spheres centred on the LG. The growth of estimated shot noise is also shown as dashed lines. The black line is the dipole reconstructed with $\beta = 0.5$. The blue line is the dipole reconstructed with $\beta = 0.5$ from the CMB redshifts. The green line is the dipole reconstructed with $\beta = 1.0$. The red line is the dipole from Erdoğdu et al. (2006) and the dashed line is the associated shot noise. Bottom plot: the angle between the CMB dipole ($l = 273^\circ$, $b = 29^\circ$) and the reconstructed LG velocity. The lines are colour coded to coincide with the top plot. The dashed lines denote the shot noise errors.

50 h^{-1} Mpc. However, the amplitude of the Wiener dipole is less than the number-weighted dipole. This is due to the fact that in the previous paper, we did not filter the shot noise errors. Furthermore, in the previous paper, we did not take peculiar velocities into account when calculating the number-weighted dipole and these will lead to the overestimation of the LG-frame dipole (the Rocket effect). The value for β we obtain by equating the CMB dipole measurements with our reconstructed dipole reflects the decrease in the amplitude. We get $\beta = 0.54 \pm 0.12$ at 13 000 km s^{-1} whereas we find $\beta = 0.40 \pm 0.09$ at 13 000 km s^{-1} in Erdoğdu et al. (2006). The convergence of the direction of the LG dipole does not seem affected by the velocity corrections but there is in general better alignment between the Wiener-reconstructed LG dipole and the CMB dipole than the LG dipole, calculated directly from the raw data and the CMB dipole. The misalignment angle of the Wiener dipole from the LG redshifts is almost as that of the raw-data dipole up to 13 000 km s^{-1} and the angle is 39° at this distance. At least half of this misalignment is probably due to the fact that when we modelled the LG dipole, we assumed all the galaxies have the same weight (see Erdoğdu et al. 2006). Also our analysis uses linear perturbation theory which is correct only to first-order δ. There may be contributions to the LG dipole from small scales which would cause gravity and the velocity vectors to misalign.

7 SUMMARY AND CONCLUSIONS

In this paper, the Wiener reconstruction technique was applied to recover real-space density and velocity fields from 2MRS. The observed density field was first expanded in terms of spherical harmonics and spherical Bessel functions (equations 4 and 6) which are both orthogonal and which together satisfy Poisson's equation. Then, the redshift distortions, described by the coupling matrix $\mathbf{Z}$, were corrected for by the matrix inversion of $\mathbf{Z}$ in equation (11), assuming linear theory and a value of $\beta = \Omega^{0.6}/b = 0.5$. After the inversion, the real-space density field was estimated using the Wiener filter for a given CDM power spectrum with $\sigma_8 = 0.7$ and $\Gamma = 0.2$ (equations 12–14). Finally, the velocity field is reconstructed from the Wiener-filtered density field using equation (9).

The reconstructed density field resolves most of the known structures as well as new clusters and voids. The density and velocity fields agree well with the *IRAS* PSCz and 1.2-Jy fields derived using the Wiener filter technique. There is a backside infall towards the Great Attractor region, in agreement with Schmoldt et al. (1999) and FLHLZ. There is a strong outflow towards the Shapley supercluster which suggests that Shapley plays an important dynamical role in the local velocity field.

The LG dipole derived from the reconstructed velocity field is lower in amplitude at all distances than the LG dipole derived from the raw data by Erdoğdu et al. (2006). The misalignment angle between the CMB dipole and the 2MRS dipole decreases down to 13° at 5000 km s^{-1} and its amplitude is about 800 β km s^{-1}. If our canonical value for β is correct then this suggests most of the acceleration is generated within 5000 km s^{-1} and the structure at higher distances contributes less than 30 per cent to the LG dipole. The 'tug of war' between the Great Attractor and the Perseus–Pisces supercluster to which the dipole is commonly attributed can clearly be seen in Fig. 11. The 2MRS dipole agrees well with the best-fitting value for the canonical model to the data with $\beta = 0.5$, for fixed $\Gamma = 0.2$ and $\sigma_8 = 0.7$.

The Wiener filter technique performs very well and provides a rigorous reconstruction method determined by the data and the expected signal. In a forthcoming paper, we will compare the reconstructed fields with the peculiar velocities from the 6dF survey. This will allow us to test the validity of our reconstructions and enable the refinement of our method.

ACKNOWLEDGMENTS

Special thanks to Peter Coles, Yehuda Hoffman, Michelle Lanyon, Karen Masters and Chris Short for their valuable comments. PE would like to thank the University College London for its hospitality during the completion of this work. OL acknowledges a PPARC Senior Research Fellowship. JPH, LMM, CSK, NM and TJ are supported by NSF grant AST-0406906, and EF's research is partially supported by the Smithsonian Institution. DHJ is supported as a Research Associate by Australian Research Council Discovery-Projects Grant (DP-0208876), administered by the Australian National University. This publication makes use of data products from the 2MASS, which is a joint project of the University of Massachusetts and the Infrared Processing and Analysis Center/California Institute of Technology, funded by the National Aeronautics and Space Administration and the National Science Foundation. This research has also made use of the NASA/IPAC Extragalactic Database (NED) which is operated by the Jet Propulsion Laboratory, California Institute of Technology, under contract with the National Aeronautics and Space Administration and the SIMBAD database, operated at CDS, Strasbourg, France.

REFERENCES

Bennett C. L. et al., 2003, ApJS, 148, 1
Branchini E. et al., 1999, MNRAS, 308, 1
Cambrésy L., Jarrett T. H., Beichman C. A., 2005, A&A, 435, 131
Cardelli J. A., Clayton G. C., Mathis J. S., 1989, ApJ, 345, 245
Cohen M., Wheaton W. A., Megeath S. T., 2003, AJ, 126, 1090
Cole S. et al., 2005, MNRAS, 362, 505
Conway E. et al., 2005, MNRAS, 356, 456
Cooray A., Sheth R., 2002, Phys. Rep., 372, 1
Courteau S., Van Den Bergh S., 1999, AJ, 118, 337
Davis M., Nusser A., Willick J., 1996, ApJ, 473, 22
Dressler A., Faber S. M., 1990, ApJ, 354, L45
Ebeling H., Mullis C. R., Tully R. B., 2002, ApJ, 580, 774
Einasto M., Tago E., Jaaniste J., Einasto J., Andernach H., 1997, A&AS, 123, 119
Erdoğdu P. et al., 2004, MNRAS, 352, 939
Erdoğdu P. et al., 2006, MNRAS, 368, 1515
Fabbri R., Natale V., 1990, ApJ, 363, 3
Fairall A. P., 1988, MNRAS, 230, 69
Fisher K. B., Scharf C. A., Lahav O., 1994, MNRAS, 266, 219
Fisher K. B., Lahav O., Hoffman Y., Lynden-Bell D., Zaroubi S., 1995, MNRAS, 272, 885 (FLHLZ)
Freedman W. L. et al., 2001, ApJ, 553, 47
Frith W. J., Outram P. J., Shanks T., 2005, MNRAS, 364, 593
Geller M., Huchra J. P., 1989, Sci, 246, 897
Hamilton A. J. S., Tegmark M., Padmanabhan N., 2000, MNRAS, 317, L23
Heavens A. F., Taylor A. N., 1995, MNRAS, 275, 483
Hoffman Y., Eldar A., Zaroubi S., Dekel A., 2001, preprint (astro-ph/0102190)
Huchra J. et al., 2005, in Fairall K. P., Woudt P. A., eds, ASP Conf. Ser., Vol. 329, Nearby Large-Scale Structures and the Zone of Avoidance. Astron. Soc. Pac., San Francisco, p. 135
Jarrett T. H., 2004, Publ. Astron. Soc. Aust., 21, 396
Jarrett T. H., Chester T., Cutri R., Schneider S. E., Skrutsie M., Huchra J. P., 2000a, AJ, 119, 2498
Jarrett T. H., Chester T., Cutri R., Schneider S. E., Rosenberg J., Huchra J. P., 2000b, AJ, 120, 298
Jarrett T. H., Chester T., Cutri R., Schneider S. E., Huchra J. P., 2003, AJ, 125, 525
Jones D. H. et al., 2004, MNRAS, 355, 747
Jones D. H., Saunder W., Read M., Colless M., 2005, Publ. Astron. Soc. Aust., 22, 277
Klemola A. R., 1969, AJ, 74, 804
Kochanek C. S. et al., 2001, ApJ, 560, 566
Kraan-Korteweg R. C., Woudt P. A., Cayette V., Fairall A. P., Balkowski C., Henning P. A., 1996, Nat, 379, 519
Lahav O., Yamada T., Scharf C., Kraan-Korteweg R. C., 1993, MNRAS, 262, 711
Lahav O., Fisher K. B., Hoffman Y., Scharf C. A., Zaroubi S., 1994, ApJ, 423, L93
Lynden-Bell D., 1993, in Babu G. B., Feigelson E. D., eds, Statistical Challenges in Modern Astronomy. Springer-Verlag, New York, p. 201
Maller A. H., McIntosh D. H., Katz N., Weinberg M. D., 2005, ApJ, 619, 147
Marinoni C. et al., 2005, A&A, 442, 801
Mathewson D. S., Ford V. L., Buchhorn M., 1992, ApJ, 389, L5
Nusser A., Davis M., 1994, ApJ, 421, L1
Peacock J. A., Dodds S., 1994, MNRAS, 267, 1020
Peebles P. J. E., 1973, ApJ, 185, 413
Peebles P. J. E., 1980, The Large-Scale Structure of the Universe. Princeton Univ. Press, Princeton, NJ
Pike R. W., Hudson M. J., 2005, ApJ, 635, 11
Porter S. C., Raychaudhury S., 2005, MNRAS, 364, 1387
Regs E., Szalay A. S., 1989, ApJ, 345, 627
Rowan-Robinson M. et al., 2000, MNRAS, 314, 375
Rybicki G. B., Press W. H., 1992, ApJ, 398, 169
Saunders W. et al., 1991, Nat, 349, 32
Saunders W. et al., 2000, MNRAS, 317, 55
Scharf C. A., Lahav O., 1993, MNRAS, 264, 439
Scharf C. A., Hoffman Y., Lahav O., Lynden-Bell D., 1992, MNRAS, 256, 229
Schlegel D. J., Finkbeiner D. P., Davis M., 1998, ApJ, 500, 525
Schmoldt I. M. et al., 1999, AJ, 118, 1146
Spergel D. N. et al. 2006, ApJ, submitted
Tadros H. et al., 1999, MNRAS, 305, 527
Taylor A. N., Ballinger W. E., Heavens A. F., Tadros H., 2001, MNRAS, 327, 689
Tegmark M. et al., 2004, ApJ, 606, 70
Valentine H., Saunders W., Taylor A., 2000, MNRAS, 319, L13
Wakamatsu K., Hasegawa T., Karoji H., Sekiguchi K., Menzies J. W., Malkan M., 1994, in Balkowski C., Kraan-Kortweg R. C., eds, ASP Conf. Ser. Vol. 67, Unveiling Large-Scale Structures Behind the Milky Way. Astron. Soc. Pac., San Francisco, p. 131
Webster M., Lahav O., Fisher K., 1997, MNRAS, 287, 425 (WLF)
Wegner G., Colless M., Saglia R. P., McMahan R., Davies R. L., Burstein D., Baggley G., 1999, MNRAS, 305, 259
White R. A., Bliton M., Bhavsar S. P., Bornmann P., Burns J., Ledlow M., Loken C., 1999, AJ, 118, 2014
Wild V. et al., 2005, MNRAS, 356, 247
Worthey G., 1994, ApJS, 95, 107
Woudt P., 1998, PhD thesis, Cape Town Univ.
Yahil A., 1994, in Suto K., ed., Evolution of the Universe and its Observational Quest. Tokyo Universal Academy Press, Japan
Yahil A., Strauss M., Davis M., Huchra J. P., 1991, ApJ, 372, 380
Zaroubi S., 2002, MNRAS, 331, 901
Zaroubi S., Hoffman Y., 1996, ApJ, 462, 25
Zaroubi S., Hoffman Y., Fisher K., Lahav O., 1995, ApJ, 449, 446
Zwicky F., Herzog E., 1966, Catalogue of Galaxies and of Clusters of Galaxies, Vol. III. California Institute of Technology, Pasadena, CA

This paper has been typeset from a TEX/LATEX file prepared by the author.